The force-sensing GPCR LPHN2 is indispensable for normal auditory function

Zhao Yang[1,2,3#], Ming-Wei Wang[4#], Shu-Hua Zhou[1,2#], Zhi-Chen Song[2#], Kong-Kai Zhu[3#], Xin Wen[1#], Qi-Yue Zhang[1#], Ying Guan[4#], Jia-Rui Gao[2#], Xiao-Hui Wang[5], Ya-Qi Wang[1], Wen-Wen Liu[6], Lei Xu[6], Wei Xiong[7], Ren-Jie Chai[8,9*], Chuan Wang[10*], Zhi-Gang Xu[11*], Xiao Yu[2*], Jin-Peng Sun[1,3,12*]

Affiliations:

[1]NHC Key Laboratory of Otorhinolaryngology, Qilu Hospital of Shandong University, and Department of Biochemistry and Molecular Biology, School of Basic Medical Sciences, Cheeloo College of Medicine, Shandong University, Jinan 250012, China.

[2]Key Laboratory of Experimental Teratology of the Ministry of Education, Department of Physiology, School of Basic Medical Sciences, Cheeloo College of Medicine, Shandong University, Jinan 250012, China.

[3]Advanced Medical Research Institute, Cheeloo College of Medicine, Shandong University, Jinan 250012, China.

[4]Department of Clinical Laboratory, The Second Hospital, Cheeloo College of Medicine, Shandong University, Jinan 250012, China.

[5]Department of Otorhinolaryngology, Union Hospital, Tongji Medical College, Huazhong University of Science and Technology, Wuhan, China.

[6]Department of Otolaryngology-Head and Neck Surgery, Shandong Provincial ENT Hospital, Cheeloo College of Medicine, Shandong University, Jinan 250014, China.

[7]Chinese Institute for Brain Research, Beijing 102206, China

[8]State Key Laboratory of Digital Medical Engineering, Department of Otolaryngology Head and Neck Surgery, Zhongda Hospital, School of Life Sciences and Technology, School of Medicine, Advanced Institute for Life and Health, Jiangsu Province High-Tech Key Laboratory for Bio-Medical Research, Southeast University, Nanjing, 210096, China.

[9]Department of Neurology, Aerospace Center Hospital, School of Life Science, Beijing Institute of Technology, Beijing, 100081, China.

[10]Department of Pharmacology, Hebei Medical University, Shijiazhuang 050000, China

[11]Shandong Provincial Key Laboratory of Animal Cells and Developmental Biology, Shandong University School of Life Sciences, Qingdao 266237, China

[12]Key Laboratory of Molecular Cardiovascular Science of the Ministry of Education, Department of Physiology and Pathophysiology, School of Basic Medical Sciences, Peking University, Beijing 100191, China.

# These authors contributed equally to this work.

* Correspondence: Jin-Peng Sun, E-mail: sunjinpeng@sdu.edu.cn

Xiao Yu, E-mail: yuxiao@sdu.edu.cn

Zhi-Gang Xu, E-mail: xuzg@sdu.edu.cn

Chuan Wang, E-mail: wangchuan@hebmu.edu.cn

Ren-Jie Chai, E-mail: renjiec@seu.edu.cn

Abstract

The conversion of force sensation into electrical signals via mechanoelectrical transduction (MET) is considered the key step in auditory perception. Here, we found that G protein-coupled receptor (GPCR) LPHN2/ADGRL2 was expressed at the tips of stereocilia in cochlear hair cells and was associated with MET channel components. Hair cell-specific LPHN2 deficiency caused hearing loss and impaired MET responses. A specific inhibitor of LPHN2, developed by in silico screening and pharmacological characterization, reversibly blocked the MET response. Mechanistically, administration of force to LPHN2 activated TMC1 through direct interaction and caused conformational changes in TMC1 in vitro. Furthermore, the sensing of force by LPHN2 stimulated Ca^{2+} responses and neurotransmitter release in hair cells. Finally, hearing loss in LPHN2-deficient mice was reversed by the re-expression of LPHN2-GAIN in cochlear hair cells. The important roles of LPHN2 in auditory perception and a TMC-coupled force sensor indicated that GPCRs could be candidate auditory receptors.

Introduction

Auditory perception is one of our basic senses and allows us to experience the features of the acoustic world, including melodious music, chirps of birds and tinkling of spring water.

Additionally, auditory perception is our main mechanism for communicating with each other via speech, and it alerts us to possible dangers. By converting mechanical force into electrical signals, previous studies have suggested that mechanoelectrical transduction (MET) in cochlear hair cells act as the central event during auditory perception (Gillespie and Muller, 2009; Hudspeth and Corey, 1977; Hudspeth and Jacobs, 1979; Kawashima et al., 2011; Pan et al., 2018; Zheng and Holt, 2021). The molecular identity of MET channels in hair cells remained elusive for decades; however, a series of candidate components of the MET channel complex, which include the transmembrane membrane proteins TMC1/2, TMIE, and LHFPL5 as well as auxiliary subunits such as calcium (Ca^{2+}) and integrin binding protein 2 and 3 (CIB2/3), were recently identified and have gradually been characterized (Cunningham et al., 2020; Giese et al., 2017; Liang et al., 2021; Pan et al., 2013; Tang et al., 2020; Wang et al., 2023; Xiong et al., 2012). In the research field of hearing, TMC1/2 are increasingly becoming recognized as the pore-forming subunits of hair cell MET channels. In addition to these MET components, which are concentrated at the tips of stereocilia, another mechanosensitive ion channel Piezo2, which is expressed at the apical surface of cochlear hair cells, has also been suggested to be a force sensor that is required for reverse-polarity currents (Wu et al., 2017).

In addition to ion channels, G protein-coupled receptors (GPCRs) are well known to function as important sensory receptors that mediate the sensation of light, odor, itch and at least three qualities of taste (Buck and Axel, 1991; Guo et al., 2023; Yang et al., 2021; Yau and Hardie, 2009; Zhang et al., 2003). Importantly, several GPCRs have been shown to be essential for hearing. For instance, CELSR1 and Fzd3/6 are required for the maintenance of cochlear planar cell polarity, and LGR5 regulates the self-renewal abilities of cochlear hair cells (Chai et al., 2012; Duncan et al., 2017; Shi et al., 2013; Wang et al., 2006). Moreover, ADGRV1 is a component of ankle links and is required for proper stereocilia development (Guan et al., 2023; Hu et al., 2014; McGee et al., 2006; Weston et al., 2004). Although GPCRs play important regulatory roles in cochlear development, it is still unknown whether GPCRs participate in direct force sensation during hearing processes, modulate membrane excitability and contribute to neurotransmitter release. In contrast to ion channels, GPCRs often modulate intracellular secondary messengers to produce sensory signals (Arshavsky and Bownds, 1992; Chandrashekar et al., 2006; Chen and Yau, 1994; Nakamura and Gold, 1987; Yang et al., 2021;

Zhang et al., 2003). Notably, the seminal work of the Hudspeth Laboratory showed that MET is an extremely rapid process that occurs within microseconds (Corey and Hudspeth, 1979). Therefore, GPCRs are generally not considered to be direct auditory receptors because of their slower kinetics. For example, the latency of the fastest known G protein signaling pathway, which is mediated by the rhodopsin-Gt-TRP channel complex and participates in Drosophila phototransduction, was measured to be ~20 ms.

In addition to the conventional secondary messenger system, we hypothesized that GPCRs may also be able to regulate acute physiological responses by directly binding to and modulating the activity of ion channels via conformational changes (Davare et al., 2001; Liu et al., 2017; Zhang et al., 2012). Therefore, it is possible that GPCRs could serve as hearing sensors and may interact with the quick initial sensation of sound that is mediated by mechanosensitive ion channels or individually trigger neurotransmitter release. We hypothesized that candidate auditory receptors (exemplified by GPCRs) may meet the following criteria: (1) the candidate is expressed in the stereocilia of cochlear hair cells; (2) the candidate directly senses force in a physiological range (2~100 dynes/cm^2); (3) the candidate can convert force stimuli to modulate the membrane potentials of hair cells, mediate changes in intracellular second messengers or regulate neurotransmitter release; and (4) knocking out the gene that encodes the candidate leads to hearing disorders in animal models. Considering these criteria, we cannot exclude the possibility that GPCRs might directly participate in auditory perception by physically interacting with MET subunits or modulating specific variants, such as amplitude or period, during hearing sensation.

In our parallel paper, we found that a mechanosensitive GPCR, LPHN2, was uniquely expressed at the apical surface of utricular hair cell, which was indispensable for normal equilibrioception of mice (Yang et al., 2024). In the present study, we showed that LPHN2 was distributed in cochlear hair cells at both the stereocilia and the apical membrane surface. Global knockout of *Lphn2* or inducible hair cell-specific LPHN2 knockout impaired the hearing of mice. Importantly, the MET current in LPHN2-expressing cochlear hair cells was impaired either by genetic ablation of LPHN2 or by pharmacological inhibition of LPHN2 with a specific inhibitor. Mechanistically, when LPHN2 sensed force, it directly coupled to TMC1 and induced conformational changes in TMC in an *in vitro* reconstitution system, and these effects occurred

independently of its Gs-activating ability. We further revealed that force sensation by LPHN2 induced Ca^{2+} signaling and transmitter release in cochlear hair cells. Overall, our findings identify a mechanosensitive GPCR that could function as a direct sensor of force during hearing by functionally coupling to TMC1; this GPCR might be a component of the mechanotransduction machinery of cochlear hair cells.

Results

Expression of LPHN2 in cochlear hair cells

Previous single-cell RNA sequencing (scRNA-seq) data revealed that LPHN2 is expressed primarily in cochlear hair cells and that its expression exhibits a dynamic pattern (Ranum et al., 2019). Our quantitative RT-PCR results revealed that the mRNA level of *Lphn2* in the mouse cochlear epithelium decreased by approximately 30% from E20 to P14 and then reached a steady-state at P30 (Figure 1A). Using the purified LPHN2 protein as a reference, the protein level of LPHN2 in cochlear hair cells was measured to be approximately 387 ± 13 fmol/mg, which is approximately 1.5-fold higher than that of VLGR1, at P10 (Figures S1A and S1B). VLGR1 is a deafness-associated GPCR and an ankle link component of hair cells (Guan et al., 2023). To determine the pattern of LPHN2 expression in the cochlea, we performed whole-mount immunostaining with a commercial anti-LPHN2 antibody; the specificity of this antibody was demonstrated in both HEK293 cells overexpressing LPHN2 and cochleae derived from *Lphn2*$^{-/-}$ mice at E18 (Figures S1C and S1D). LPHN2 expression was detected in approximately 80% of both outer hair cells (OHCs) and inner hair cells (IHCs) throughout the length of the cochlear duct at P10, and there were no significant tonotopic differences in the apical, middle or basal turns (Figure 1B).

Importantly, via separation of stereocilia from the hair cell body using a modified twist-off method (Avenarius et al., 2017), we were able to detect LPHN2 expression in both the stereocilia and the cell bodies of cochlear hair cells using TMIE/PCDH15 and Myosin7a as markers of stereocilia and cell bodies, respectively (Figures 1C and S1E-S1G). The results showed that LPHN2 was expressed only in the cell body but not in the stereocilia of utricular hair cells, which was consistent with the immunostaining results of our parallel study (Figures 1C and S1E-S1G). To further explore the subcellular expression pattern of LPHN2, we

150 collected different optical sections ranging from the stereocilia to the cochlear hair cell body
151 and examined the localization of LPHN2 (Figure 1D). Notably, in both the cochlear OHCs and
152 IHCs of mice at P10, immunofluorescence puncta indicating LPHN2 were observed along the
153 stereocilia, with staining at the tips of several shorter rows of stereocilia but not in the longest
154 stereocilia (Figure 1E). LPHN2 immunofluorescence was also observed at the apical surfaces
155 above the cuticular plate of HCs; this conclusion was supported by the close proximity of
156 LPHN2 to spectrin, which is a specific marker of the cuticular plate, and by the results of
157 staining sections of the cochlear sensory epithelium with an antibody against Myosin7a, which
158 is a marker of hair cells (Figures 1F and S1H). In contrast, LPHN2 was not expressed at the
159 basolateral membrane along the cell bodies of HCs (Figure 1F). To exclude the possibility of
160 antibody nonspecificity, we detected LPHN2 expression in whole mounts of cochlea derived
161 from a transgenic knock-in mouse line in which the C-terminus of LPHN2 is tagged with an
162 mCherry sequence (LPHN2^{mCherry} mice) (Figure S1I). Consistent with the immunostaining data,
163 LPHN2-mCherry was also expressed at the tips of shorter rows of stereocilia as well as at the
164 apical surface of both IHCs and OHCs (Figures 1G and S1J). The specific expression pattern
165 of the mechanosensitive receptor LPHN2 in cochlear hair cells, especially its localization at the
166 tips of stereocilia, suggests that LPHN2 might perform unique functions in the auditory system.
167

168 **LPHN2 deficiency severely impairs hearing**

169 To investigate the functional roles of LPHN2 in hearing, we initially used heterozygous
170 *Lphn2* gene-knockout (*Lphn2*$^{+/-}$) mice since homozygous knockout of this gene (*Lphn2*$^{-/-}$ mice)
171 results in embryonic lethality (Anderson et al., 2017) (Figures S2A-S2C). *Lphn2*$^{+/-}$ mice are
172 viable and exhibit normal growth, but vestibular defects were observed in these mice in our
173 parallel study (Yang et al., 2024). Measurement of the auditory brainstem response (ABR)
174 revealed that at P30, *Lphn2*$^{+/-}$ mice had an ~30 dB higher auditory threshold in response to click
175 stimuli than did their wild-type (WT) littermates (Figure S2D). Moreover, compared with those
176 of WT mice, *Lphn2*$^{+/-}$ mice exhibited significantly elevated ABR thresholds at different
177 frequencies (4, 8, 12, 16, 24 and 32 kHz) (Figures S2D and S2E). ABR wave I analysis further
178 indicated a decreased wave amplitude and increased wave latency in *Lphn2*$^{+/-}$ mice, suggesting
179 that the function of IHC synapses was impaired in *Lphn2*$^{+/-}$ mice (Figure S2F). Furthermore,

180 the threshold of distortion product otoacoustic emission (DPOAE) in *Lphn2*$^{+/-}$ mice was
181 significantly increased between 12 and 24 kHz, suggesting that OHC function was affected in
182 *Lphn2*$^{+/-}$ mice (Figure S2G). Since the deterioration of hearing function might occur due to
183 developmental defects in hair cells, we examined hair cell morphology by immunostaining and
184 scanning electron microscopy. The results of both analyses revealed no detectable impairment
185 in the structure or morphology of OHCs or IHCs in the cochleae of *Lphn2*$^{+/-}$ mice, suggesting
186 that the heterozygous ablation of LPHN2 in mice did not cause developmental defects in
187 cochlear hair cells, at least at the age of 4 weeks (Figures S2H-S2J).

188 To further assess the specific role of LPHN2 in cochlear hair cells, we crossed *Lphn2*$^{fl/fl}$ mice
189 with an inducible *Pou4f3-CreER*$^{+/-}$ transgenic mouse line (Figure S2K). Previous scRNA-seq
190 data (GSE114157) indicated that POU4F3, which is a commonly used marker of hair cells, is
191 expressed in all LPHN2-positive cochlear hair cells; therefore, we used *Pou4f3-CreER*$^{+/-}$
192 *Lphn2*$^{fl/fl}$ mice to knockout LPHN2 specifically in hair cells. Consistently, the specific knockout
193 of LPHN2 in the cochleae and utricles of *Pou4f3-CreER*$^{+/-}$*Lphn2*$^{fl/fl}$ mice was confirmed by both
194 immunofluorescence staining and western blotting (Figures S2L-S2N). In contrast, LPHN2
195 expression in other tissues, such as the brain, was not significantly affected in *Pou4f3-CreER*$^{+/-}$
196 *Lphn2*$^{fl/fl}$ mice (Figures S2L and S2M). Notably, compared with their control *Pou4f3-CreER*$^{+/-}$
197 *Lphn2*$^{+/+}$ littermates, *Pou4f3-CreER*$^{+/-}$*Lphn2*$^{fl/fl}$ mice exhibited severe hearing impairment, as
198 indicated by an elevated ABR threshold at all testing frequencies and deterioration of DPOAE
199 between 8 and 32 kHz (Figures 2A-2D). As in *Lphn2*$^{+/-}$ mice, *Pou4f3-CreER*$^{+/-}$*Lphn2*$^{fl/fl}$ mice
200 exhibited normal cochlear hair cell structure and morphology at P30 (Figures 2E, 2F and S2O).
201 In addition, the expression levels and the localization of MET machinery components,
202 including TMC1, TMC2, TMIE, LHFPL5 and PCDH15, in the cochlear hair cells of *Pou4f3-*
203 *CreER*$^{+/-}$*Lphn2*$^{fl/fl}$ mice were comparable to those in their wild-type littermates (Figure 2G).
204 Collectively, these findings support the idea that LPHN2 expressed in cochlear hair cells is
205 indispensable for normal hearing.

206

207 **Force sensation by LPHN2 induces changes in second messengers in cochlear hair cells**

208 GPCRs act as direct sensors of itch and participate in the senses of vision, smell, and taste
209 by converting extracellular stimuli into changes in the intracellular levels of second messengers,

210 such as cAMP, cGMP and Ca^{2+} (Filipek et al., 2003; Guo et al., 2023; Kaupp, 2010; Smith,
211 2023; Yang et al., 2021; Yang et al., 2023). Our parallel study indicated that LPHN2 activated
212 Gs and Gi signaling in response to force stimulation (Figures S3A and S3B). We therefore
213 measured cAMP levels after the delivery of force to LPHN2 using paramagnetic beads that
214 were coated with an anti-LPHN2 antibody (LPHN2-M-beads). This antibody recognizes the N-
215 terminus (residues 551-600) of LPHN2 and can exert quantifiable force on LPHN2 in a
216 magnetic field (Figure 3A). In the heterologous system, we showed that upon the application
217 of magnetic force, LPHN2-M-beads induced a dose-dependent increase in the cAMP
218 concentration in LPHN2-overexpressing HEK293 cells but not in cells that were transfected
219 with the empty vector pcDNA3.1 (Figures 3B and S3C). The EC50 for the LPHN2-M-bead-
220 induced increase in cAMP concentrations in vitro was 1.70 ± 0.34 pN. In contrast, polylysine-
221 coated paramagnetic beads (Ctrl-beads) did not increase the cAMP concentrations in LPHN2-
222 expressing HEK293 cells in response to the application of force, thus supporting the specificity
223 of the LPHN2-M-beads in activating LPHN2 (Figure 3B). We subsequently applied LPHN2-
224 M-beads to murine cochlear explants. The results revealed that the application of 3 pN force to
225 cochlear sensory epithelium harvested from *Pou4f3-CreER*$^{+/-}$*Lphn2*$^{+/+}$ mice induced an
226 approximately 1.6~2.2-fold increase in intracellular cAMP levels in different sections (apical
227 turn: from 1.49 ± 0.11 mM to 2.41 ± 0.13 mM; middle turn: from 1.58 ± 0.07 mM to 3.41 ±
228 0.18 mM; basal turn: from 1.51 ± 0.08 mM to 2.48 ± 0.14 mM); these effects of force were
229 suppressed in cochlear explants that were pretreated with the nonspecific Gs inhibitor NF449
230 or in cochlear explants from *Pou4f3-CreER*$^{+/-}$*Lphn2*$^{fl/fl}$ mice at P10 (Figure 3C). In contrast, the
231 force applied by Ctrl-beads did not induce detectable changes in cAMP concentrations in
232 cochlear explants (Figure S3D). These results suggest that the Gs-cAMP pathway downstream
233 of LPHN2 is activated in response to force stimulation in the cochlea. Consistent with these
234 findings, Gs was the most abundantly expressed G protein subtype in LPHN2-expressing
235 cochlear hair cells, as revealed by both scRNA-seq data and single-cell qRT–PCR analysis of
236 20 isolated cochlear hair cells (Figures 3D and S3E).

237 Notably, the intensity of the force that was applied by magnetic beads in this study was
238 determined based on our calculation that 10 pN equals 100 dynes/cm^2 on the plasma membrane
239 of stereocilia or the apical surface of hair cells; this approach was used in a previous study to

240 mimic arterial wall shear stress (approximately 1 m/s under physiological conditions) (Mehta
241 et al., 2020). Therefore, the force of 1.7~10 pN that was used in the present study was within
242 the physiological range, mimicking approximately 17 cm/s ~100 cm/s fluid velocity.
243

244 **LPHN2 deficiency impairs the MET current in cochlear hair cells**

245 The localization of LPHN2 at the tips of shorter rows of stereocilia in cochlear hair cells, the
246 observation of auditory defects in *Lphn2*-deficient mice, and the lack of abnormalities in hair
247 bundle development or MET component assembly in *Lphn2*-deficient mice collectively suggest
248 that LPHN2 might directly participate in auditory perception. We therefore investigated
249 whether LPHN2 participates in MET by performing whole-cell voltage-clamp recording
250 experiments. In these experiments compared recordings of mid-apical cochlear hair cells
251 derived from *Pou4f3-CreER*$^{+/-}$*Lphn2*$^{fl/fl}$ mice with those of cells derived from wild-type
252 littermate mice in response to deflection of hair bundles by a fluid jet (Figure 4A). To record
253 MET currents specifically in LPHN2-expressing hair cells, we administered a modified AAV-
254 ie-*Lphn2pr*-mCherry to P3 mice via round window membrane injection (Figure 4A). The
255 efficiency of mCherry labeling and accuracy of viral targeting of LPHN2-expressing cells were
256 validated by both immunostaining with an anti-LPHN2 antibody and single-cell RT–PCR
257 (Figures S4A and S4B).

258 The cochleae of AAV-treated mice were isolated at P10, and mCherry-labeled hair cells were
259 selected to record macroscopic MET currents at a holding potential of -80 mV. In the LPHN2-
260 expressing OHCs from control *Pou4f3-CreER*$^{+/-}$*Lphn2*$^{+/+}$ mice, the excitatory stimuli at
261 maximal deflection elicited peak MET currents of 741.6 ± 25.4 pA (Figures 4B and 4C). In
262 contrast, compared with those of control littermates, the peak MET currents in the mCherry-
263 labeled OHCs from *Pou4f3-CreER*$^{+/-}$*Lphn2*$^{fl/fl}$ mice were reduced by approximately 70% (to
264 235.9 ± 83.3 pA) (Figures 4B and 4C). Similar defective MET currents were also observed in
265 LPHN2-expressing IHCs from *Pou4f3-CreER*$^{+/-}$*Lphn2*$^{fl/fl}$ mice (*Pou4f3-CreER*$^{+/-}$*Lphn2*$^{fl/fl}$
266 216.4± 65.1 pA vs. *Pou4f3-CreER*$^{+/-}$*Lphn2*$^{+/+}$ 679.7 ± 23.1 pA) (Figures 4B and 4C). These
267 results indicated that LPHN2 plays important roles in normal mechanotransduction in cochlear
268 hair cells.
269

Development of a selective LPHN2 inhibitor that antagonizes its force sensation

In addition to genetic LPHN2 knockout, a reversible and selective inhibitor of LPHN2 that antagonizes its force sensation could be a very useful tool for investigating how LPHN2 participates in hearing sensation and MET, and such an inhibitor could exclude the possibility of developmental defects caused by genetic ablation. We therefore constructed an inactive LPHN2 structural model according to the inactive CD97 structure that we recently solved, and we rationally designed an in-silico screening strategy to search for LPHN2 inhibitors (Figure 5A) (Mao et al., 2024a). A total of 1000,000 compounds with diverse skeleton types in a designed compound database were docked into the predicted top binding pocket of inactive LPHN2 to identify the top 5000 small molecules according to docking scores (Figure 5B). To achieve high selectivity, we filtered 5000 compounds according to their interactions with specific residues (I855, E894, F921, L1055, and T1070) in the LPHN2 pocket, because these five residues are not well conserved among aGPCR families (Figure S5A). After performing cluster analysis of the top 300 small molecules, we identified 48 compounds that exhibited high structural diversity (Figure 5B). We then performed the BRET-based G protein dissociation assay with LPHN2-overexpressing HEK293 cells, and we determined that one of these compounds, namely D11, inhibited 3 pN force-induced LPHN2 activation in a concentration-dependent manner, with an EC50 of 39.88 ± 16.24 nM (Figures 5C-5E). To further predict the binding mode of D11 to LPHN2, we performed computational simulation using a Ligand Docking panel inserted in Maestro. D11 was modeled in the orthosteric pocket of LPHN2 and exhibited a slanted V-shaped configuration (Figure 5F). Twelve hydrophobic residues (L890$^{2.57}$, F897$^{2.64}$, I901^{ECL1}, L917$^{3.36}$, F921$^{3.40}$, F925$^{3.44}$, W983^{ECL2}, L1047$^{6.49}$, W1051$^{6.53}$, L1055$^{6.57}$, F1057^{ECL3}, and F1069$^{7.42}$) and three polar residues (E894$^{2.61}$, N1073$^{7.46}$ and Q1076$^{7.49}$) from TM2-TM3, TM6-TM7 and ECL1-ECL3 of LPHN2 formed the potential D11 binding pocket (Figures 5F and 5G). In particular, the carboxyl oxygen in thiazide ring of D11 formed polar interactions with the side chain oxygen atom of E894$^{2.61}$ and side chain nitrogen atom of N1073$^{7.46}$ (Figure 5G). The trifluoromethylbenzene ring of D11 formed π-π interactions with F897$^{2.64}$ and W983^{ECL2} of LPHN2 (Figure 5G). Besides, the trifluoromethylbenzene ring of D11 formed hydrophobic interactions with I901^{ECL1}, L917$^{3.36}$, L1055$^{6.57}$, F1057^{ECL3}, and F1069$^{7.42}$. The 1,4-dimethoxyphenyl group inserted in a hydrophobic pocket composed by L890$^{2.57}$,

300 F921$^{3.40}$, F925$^{3.44}$, L1047$^{6.49}$ and W1051$^{6.53}$. Consistently, mutations in residues of the D11
301 binding pocket, such as E894$^{2.61}$A, F921$^{3.40}$A, W983^{ECL2}A or F1069$^{7.42}$A, but not mutations in
302 other randomly selected surrounding residues, abolished the inhibitory effects of D11 on force-
303 induced LPHN2 activation (Figures 5H, S5B and S5C). Importantly, D11 inhibited only force-
304 induced LPHN2 activation, and it did not have detectable effects on either the force-induced or
305 agonist-induced activation of other adhesion GPCRs in the heterologous HEK293
306 overexpression system (Figure 5I). These results suggested that D11 is a selective LPHN2
307 inhibitor. Overall, we identified a specific blocker of force sensation by LPHN2 through a
308 rationally designed in silico screening method.
309

310 **LPHN2 regulates the MET current in a Gs-independent manner**

311 We next exploited the reversible LPHN2-specific inhibitor D11 to investigate the immediate
312 mechanism by which LPHN2 contributes to MET currents in OHCs from the mid-apical turn
313 of WT cochlea in response to fluid jet stimulation. Since recent transcriptomic and functional
314 studies at the single-cell level revealed heterogeneity among cochlear hair cells, which might
315 be correlated with the tonotopic mapping of the cochlea (Frank et al., 2009; Petitpre et al., 2022;
316 Shi et al., 2023), we also examined the expression levels of key components, including *Lphn2*,
317 *Tmc1* and *Gnas*, in each of these tested cells by single-cell qRT-PCR (Figure 6A). Despite the
318 fact that the baseline MET currents were normal, none of the *Lphn2*-negative hair cells (18.7%
319 of the total) exhibited any detectable response to treatment with 50 nM D11, which was
320 consistent with the high selectivity of D11 that was observed in the in vitro biochemical assays
321 (Figures 6B and 6C). Intriguingly, among *Lphn2*-positive hair cells, hair cells that exclusively
322 expressed *Lphn2* but not those that expressed *Tmc1* (*Lphn2*+*Tmc1*-, 5.3% of the total) showed
323 no significant response to D11 treatment (Figures 6B and 6C). In contrast, MET currents in hair
324 cells that expressed both *Lphn2* and *Tmc1* (*Lphn2*+*Tmc1*+, 76% of the total) were reduced by
325 approximately 35% in response to treatment with 50 nM D11 and returned to normal after D11
326 was washed out (Figures 6B-6C and S6A-S6B). These results not only suggest that LPHN2
327 participates in the MET process but also suggest an interplay between LPHN2 and TMC1 in
328 force sensation. Consistent with this hypothesis, the inhibitory effects of D11 on the MET
329 response to fluid jet stimulation were abolished in cochlear hair cells that were harvested from

330 *Pou4f3-CreER*$^{+/-}$*Lphn2*$^{fl/fl}$ mice or from *Tmc1*$^{-/-}$ mice (Figures 6D and 6E).

331 We next explored the potential contribution of the Gs-cAMP pathway to the LPHN2-
332 regulated MET response. Notably, no significant difference was observed between the baseline
333 MET currents of Gs-positive (*Lphn2*+*Tmc1*+*Gnas*-, ~30% of the total) and Gs-negative
334 (*Lphn2*+*Tmc1*+*Gnas*+, ~45% of the total) hair cells (718.7 pA vs. 716.9 pA) or between the
335 D11-induced reduction in MET currents in these two types of cells (50% vs. 51%) (Figures S6C
336 and S6D). Therefore, LPHN2 may regulate MET currents in a Gs-independent manner.
337 Consistently, neither the genetic ablation of Gs in *Pou4f3-CreER*$^{+/-}$*Gnas*$^{fl/fl}$ mice nor the
338 pharmacological inhibition of Gs activity with the nonspecific Gs inhibitor NF449 significantly
339 affected the inhibitory effects of D11 on the MET currents in cochlear hair cells (Figures 6D-
340 6E and S6E- S6G). Collectively, these data suggest that the acute MET process that is regulated
341 by the mechanosensitive receptor LPHN2 occurs in a TMC1-dependent and Gs-cAMP-
342 independent manner.

343

344 **Colocalization and association of LPHN2 with the TMC1 complex**

345 To further delineate the mechanism by which LPHN2 participates in the MET process, we
346 next performed proteomic analyses to investigate the interactome of LPHN2 in mouse cochleae.
347 The Flag-tagged LPHN2-GAIN construct showed mechanosensitive potential that was
348 comparable to that of full-length LPHN2 (Figures 7A, S7A and S7B). We then purified the
349 Flag-tagged LPHN2-GAIN protein from the baculovirus-*Spodoptera frugiperda* (Sf9) insect
350 cell system and used the purified receptor as bait to search for potential candidates that
351 coordinate LPHN2 function in vivo (Figure 7A). Notably, several components of the MET
352 channel complex, including TMC1 and PCDH15, were detected in the complexes that were
353 precipitated from cochlear homogenates by LPHN2-GAIN-bait but not in those that were
354 precipitated by control bait (empty anti-Flag M2 beads) (Figures 7B and 7C). The interactions
355 between LPHN2 and the proteins mentioned above as well as other known MET channel
356 components, such as TMIE and LHFPL5, were further supported by an in vivo
357 coimmunoprecipitation assay that was performed with commercially available antibodies
358 (Figure 7D). Our in vitro coimmunoprecipitation experiments using a HEK293 cell
359 overexpression system further confirmed the direct interaction between LPHN2 and TMC1

360 (Figure S7C). Moreover, LPHN2 exhibited significant coimmunostaining with these MET
361 channel components at the shorter rows of stereocilia in cochlear hair cells at P10, suggesting
362 that LPHN2 may directly associate with the MET channel complex *in vivo* (Figures 7E and 7F).
363

364 **Functional coupling of the mechanosensitive receptor LPHN2 to TMC1**

365 The potential association of LPHN2 with TMC1, which is the putative pore-forming subunit
366 of the MET channel, prompted us to further investigate the functional interplay of these two
367 membrane proteins. Thus, we attempted to reconstitute the functional coupling of LPHN2 and
368 TMC1 in the heterologous HEK293 cell system. However, it is well known that TMC1 does
369 not traffic properly to the plasma membrane when it is expressed in cultured cells (Beurg et al.,
370 2015; Jia et al., 2020; Zhao et al., 2014). GPCRs are known to transport or recruit many
371 cytoplasmic proteins, including but not limited to G proteins, arrestins, GRKs and especially
372 PDZ domain-containing proteins, to the cell membrane of cochlear hair cells (Guan et al., 2023;
373 Hall et al., 1998; Komolov et al., 2017; Shukla et al., 2014). We therefore screened the ability
374 of the top 50 most highly expressed GPCRs in cochlear hair cells to transport TMC1 to the
375 plasma membrane. Interestingly, two GPCRs, namely, GPCR-hc1 and GPCR-hc2, were found
376 to transport TMC1 to the cell membrane when individually coexpressed with TMC1 in HEK293
377 cells, and GPCR-hc1 showed greater efficiency than GPCR-hc2 (Figures 8A, 8B and S7D).
378 These two GPCRs that were identified provided useful tools for further investigating the
379 electrophysiological properties of the interaction between LPHN2 and TMC1 in vitro.

380 We next performed patch-clamp recording on HEK293 cells that were cotransfected with
381 GPCR-hc1 and TMC1, and we observed spontaneous single-channel opening at a holding
382 potential of -40 mV (Figure 8C). As a negative control, HEK293 cells that were transfected
383 with only TMC1 or GPCR-hc1 showed no detectable single-channel events, thus excluding the
384 possibility that the recordings were from other unknown ion channels potentially mobilized by
385 GPCR-hc1 (Figure 8C). The all-point histogram of single-channel opening events indicated that
386 the average single-channel TMC1 current was 3.6 ± 0.2 pA, and the probability of TMC1
387 opening was 0.06 ± 0.01 (Figure 8D). The spontaneous single-channel events in HEK293 cells
388 that coexpressed TMC1 and GPCR-hc1 were voltage dependent when a series of voltage steps
389 from -100 mV to +100 mV were applied (Figures 8E and S7E). The average conductance was

390 determined to be 82.3 ± 6.4 pS, which was similar to that reported for mouse TMC1 in apical
391 cochlear hair cells in vivo (84.8~88 pS) (Beurg et al., 2018; Fettiplace et al., 2022) (Figure 8E).
392 Importantly, spontaneous single-channel events in HEK293 cells that coexpressed TMC1 and
393 GPCR-hc1 were markedly inhibited or abrogated by pretreatment with known MET channel
394 blockers, such as FM1-43 (3 μM), amiloride (0.2 mM) or dihydrostreptomycin (0.2 mM)
395 (Figure S7F). These experimental results collectively suggested that TMC1 was rendered
396 functional by coexpression with GPCR-hc1 in the heterologous HEK293 cell system.
397 To further examine whether the sensing of force by LPHN2 regulates the activity of TMC1,
398 we applied LPHN2-M-beads to the heterologous HEK293 cell reconstitution system
399 coexpressing TMC1, LPHN2 and GPCR-hc1, and we recorded single-channel opening events
400 in response to the application of 10 pN force in a magnetic field; this force equals to 100
401 dynes/cm^2 on the plasma membrane and mimics physiological stimulation at a velocity of
402 approximately 1 m/s. By resolving the single-channel currents, we observed an approximately
403 2.2-fold increase in the probability of TMC1 opening in HEK293 cells that coexpressed GPCR-
404 hc1, LPHN2 and TMC1 in response to force stimulation compared with that resting conditions
405 (Figures 8F and 8J). However, the single-channel current amplitude was not significantly
406 affected by the administration of force via LPHN2-M-beads (Figure S7G). As a negative control,
407 no force-induced single-channel events were observed in HEK293 cells that coexpressed
408 GPCR-hc1 with LPHN2 or TMC1 alone or in cells that coexpressed GPCR-hc1 with both
409 CDH23 and TMC1 (Figures S7H and S7I). Importantly, the LPHN2 mediated force-induced
410 single-channel opening was abolished by pretreatment with the LPHN2-specific inhibitor D11
411 (50 nM) or the TMC1 inhibitor amiloride (0.2 mM), but it was not significantly affected by
412 pretreatment with the nonspecific Gs inhibitor NF449 (20 μM) (Figures 8G-8J and S7J-S7K).
413 Intriguingly, an approximately 1.6-fold increase of single-channel currents was also observed
414 in HEK293 cells co-expressing GPCR-hc1, PCDH15 and TMC1 in response to 10 pN force
415 stimulation via PCDH15-M-beads, but not in samples stimulated with control beads (Figures
416 S7M and S7N). The TMC1 current was increased by approximately 2.6-fold when LPHN2 was
417 further co-expressed in this system (GPCR-hc1, PCDH15 and TMC1) (Figures S7M and S7N).
418 Therefore, these in vitro data showing that LPHN2 activates TMC1 in response to force
419 stimulation are consistent with the functional and colocalization data from the in vivo

experiments, suggesting that LPHN2 can convert extracellular mechanical stimuli to activate TMC1 in a Gs-independent manner. The LPHN2-mediated moderate increase of TMC1 open probability and its up-regulatory effect on PCDH15-induced TMC1 activation collectively imply that LPHN2 may be a component of MET machinery that modulate the tip-link-mediated MET process in sound sensation.

Force sensation by LPHN2 induces conformational changes in TMC1

The results of colocalization and co-IP of LPHN2 and TMC1 suggested that LPHN2 directly interacts and forms a complex with TMC1. To elucidate the mode of interaction between the seven transmembrane receptor LPHN2 and the ten transmembrane ion channel TMC1, we performed a BRET assay by inserting Nanoluc luciferase (Nluc) at specific positions in the intracellular loops (ICLs) or C-terminus of LPHN2 (denoted as LPHN2-ICL1/2/3-Nluc or LPHN2-C-Nluc, respectively) and adding a YFP tag to the N- or C-terminus of TMC1 (denoted as TMC1-N-YFP and TMC1-C-YFP, respectively) (Figure 9A). This method has been used to characterize the interaction between GPCRs or between GPCRs and regulatory molecules in previous studies (Angers et al., 2000; Fu et al., 2021; Guan et al., 2023; Harikumar et al., 2012). Specific saturation BRET signals were detected between LPHN2-ICL1/2-Nluc and TMC1-C-YFP in HEK293 cells (coexpressing GPCR-hc1 as described above), and these signals depended on the channel expression level; however, such signals were not detected between the other BRET pairs, suggesting that the ICL1/2 (or potentially TM1-4) region of LPHN2 is in proximity to the C-terminus or TM10 region of TMC1 (Figures 9B-9C and S8A). Moreover, the application of force to LPHN2 increased the BRET signal between LPHN2-ICL1-Nluc and TMC1-C-YFP in a dose-dependent manner, with an EC50 of 5.2 ± 1.1 pN; this value was similar to the EC50 of force-induced TMC1 activation via LPHN2 in the heterologous system (Figures 9D and 9E). Notably, the $BRET_{50}$ value for LPHN2-Nluc and TMC1-YFP was recorded when the interacting pairs were expressed at a 1:2 expression ratio, suggesting a 1:2 stoichiometry in the LPHN2-TMC1 heteromer.

To investigate force-induced conformational changes in TMC1, we added Nluc to the N-terminus of TMC1 and inserted FlAsH probes (CCPGCC) into specific positions of the ICLs to generate a panel of TMC1 conformational sensors (Figure 9F). Such conformational sensors

are often used to probe conformal changes in membrane proteins (Fu et al., 2021; Lin et al., 2022; Yang et al., 2021; Yang et al., 2024). In response to the application of force on LPHN2, the intramolecular BRET signals between the N-terminus and the ICL1, ICL2, or ICL3 of TMC1 decreased, suggesting the dissociation of these ICLs from the N-terminus (Figures 9G and S8B). In contrast, a significant increase in the BRET signal was observed at ICL4, indicating that this specific structural element moved close to the N-terminal Nluc (Figure 9G). A similar result was also observed when Nluc was fused to the ICL4 of TMC1 and the FlAsH probe was inserted in the ICL2 or ICL3; these data suggested that a separation between ICL2/3 and ICL4 of TMC1 in response to the application of force to LPHN2 (Figures 9H and S8C). Importantly, the cryo-EM structure of the *C. elegans* TMC1 complex suggests that the putative ion-conduction pathway of TMC1 mainly includes TM4-TM8 (Jeong et al., 2022). Here, we observed that in TMC1, ICL2/3 moved in an opposite direction compared with ICL4 in response to force sensation by LPHN2. This conformational change in TMC1 indicates a separation between the TM4-7 and TM8-9 ends, which indicates the potential opening of the ion channel pore (Figure 9I). RNAi-mediated knockdown of Gs or administration of the nonspecific Gs inhibitor NF449 had no significant effect on the conformational changes in TMC1. In contrast, the LPHN2-specific inhibitor D11 suppressed these conformational changes (Figure 9I). Collectively, our results suggest that LPHN2 converted force stimulation into conformational changes in TMC1 in a Gs-independent manner, and this effect was potentially mediated through physical interactions that led to the opening of the ion-conduction pore of TMC1.

Force sensation by LPHN2 stimulates a Ca^{2+} response and neurotransmitter release in cochlear hair cells

It is suggested that in response to acoustic stimulation, neurotransmitters such as glutamate are released from the ribbon synapse and regulate the excitability of spiral ganglion neurons (SGNs), which transmit sound information from cochlear hair cells to the central nervous system (Qiu and Muller, 2022; Sun et al., 2018). To explore the potential effects of force stimulation via LPHN2 on glutamate release from cochlear hair cells, we employed the red fluorescent glutamate sensor R^{ncp}-iGluSnFR (R^{ncp}-iGlu) under the control of the *hSyn* promoter,

480 which enables specific expression of this sensor in SGNs and recording of glutamate release in
481 real time (Figure 10A) (Wu et al., 2018). Notably, repeated application of force to the cochlear
482 sensory epithelium by LPHN2-M-beads resulted in marked glutamate secretion, with an EC50
483 of 5.1 ± 0.9 pN, and this glutamate secretion was inhibited by pretreatment with the LPHN2-
484 specific inhibitor D11 (Figures 10B-10D). As a negative control, the force that was applied by
485 Ctrl-beads to WT hair cells or by LPHN2-M-beads to hair cells from *Pou4f3-CreER*$^{+/-}$*Lphn2*$^{fl/fl}$
486 mice did not induce any detectable glutamate secretion (Figures S9A and S9B).
487 Neurotransmitter release from cochlear hair cells is often regulated by intracellular Ca^{2+}
488 concentrations; these concentrations are hypothesized to increase locally near the afferent
489 synapse in response to mechanical stimulation via the formation of Ca^{2+} nanodomains (Jaime
490 Tobon and Moser, 2023; Meyer et al., 2009). To record the force-induced Ca^{2+} response at the
491 single-cell level, P10 cochleae from mice that were treated with modified AAV-ie-*Lphn2pr*-
492 mCherry were isolated, and LPHN2-expressing (mCherry-labeled) hair cells were selected for
493 Ca^{2+} imaging using a Fura-2 probe (Figure 10E). Approximately 25% of the LPHN2-expressing
494 OHCs exhibited a significant Ca^{2+} response to LPHN2-M-bead-mediated force stimulation (the
495 response rate might have been affected by the efficiency with which the LPHN2-M-beads
496 bound to endogenous LPHN2 on stereocilia) (Figures 10F and 10G). In contrast, neither the
497 unlabeled cochlear hair cells nor the mCherry-labeled hair cells derived from the *Pou4f3-*
498 *CreER*$^{+/-}$*Lphn2*$^{fl/fl}$ mice produced detectable Ca^{2+} signals in response to force application,
499 suggesting the specificity of the mechanical force-mediated Ca^{2+} response via LPHN2
500 activation (Figures 10F and 10G). The force-stimulated Ca^{2+} response in LPHN2-expressing
501 cochlear hair cells was inhibited by pretreatment with the LPHN2-specific inhibitor D11 in a
502 concentration-dependent manner, and the EC50 value was 18 ± 1 nM; this result was similar to
503 the inhibitory effect of D11 on force-stimulated LPHN2 activation in the heterologous system,
504 suggesting the specificity of LPHN2 in mediating the force-induced Ca^{2+} response (Figures
505 10H and S9C-S9D). Notably, in our previous proteomic analyses, we found that in addition to
506 its association with MET channel components, LPHN2 also interacted with other cation
507 channels, such as CNGA3, whose activity is regulated by cyclic nucleotides. Therefore, upon
508 the sensing of force, LPHN2 might also activate CNGA3 through Gs-dependent cAMP
509 upregulation. However, further studies are warranted to evaluate the potential contribution of

510 TMC1-dependent and/or Gs-dependent signaling to the force-induced Ca^{2+} response in
511 cochlear hair cells through LPHN2 activation. Nevertheless, our results indicated that LPHN2
512 directly participates in the MET process in cochlear hair cells and converts force stimulation
513 into an intracellular Ca^{2+} response, leading to neurotransmitter release and potential regulation
514 of SNG excitability.
515

516 **LPHN2 re-expression in cochlear hair cells of *Lphn2*-deficient mice reverses hearing loss**

517 To further validate the functional roles of LPHN2 in the peripheral auditory system,
518 especially in cochlear hair cells, we next performed an in vivo rescue experiment. In particular,
519 we delivered LPHN2-encoding AAV-ie into the cochleae of *Pou4f3-CreER*$^{+/-}$*Lphn2*$^{fl/fl}$ mice and
520 examined its effects on the auditory functions of these *Lphn2*-deficient mice. The LPHN2-
521 GAIN construct, which lacked the 523 N-terminal residues but retaining force sensation ability
522 (Figures S7A and 7B), was packaged into the AAV-ie-*Lphn2pr*-mCherry vector (referred to as
523 AAV-ie-*Lphn2pr*-LPHN2) and delivered into P3 *Pou4f3-CreER*$^{+/-}$*Lphn2*$^{fl/fl}$ mice by round
524 window membrane injection (Figure S10A). LPHN2-GAIN was specifically expressed in the
525 cochleae and vestibules, but not in the brain, of virus-treated *Pou4f3-CreER*$^{+/-}$*Lphn2*$^{fl/fl}$ mice, as
526 shown via western blotting (Figure S10B). In particular, LPHN2 was re-expressed at the tips of
527 shorter rows of stereocilia in both cochlear OHCs and IHCs of AAV-ie-*Lphn2pr*-LPHN2-
528 treated *Pou4f3-CreER*$^{+/-}$*Lphn2*$^{fl/fl}$ mice (Figures S10C-S10E). In contrast, no LPHN2-GAIN
529 expression was observed in the cochleae of *Pou4f3-CreER*$^{+/-}$*Lphn2*$^{fl/fl}$ mice that were treated
530 with the AAV-ie-*Lphn2pr*-mCherry control virus (Figures S10C-S10E).

531 We next assessed the auditory functions of mice that were subjected to LPHN2-GAIN or
532 control gene delivery. Notably, *Lphn2*-deficient mice that were treated with AAV-ie-*Lphn2pr*-
533 LPHN2 exhibited significantly improved performance in the ABR test. The ABR thresholds at
534 all the testing frequencies, as well as the amplitude and latency of ABR wave I, of AAV-ie-
535 *Lphn2pr*-LPHN2-treated *Pou4f3-CreER*$^{+/-}$*Lphn2*$^{fl/fl}$ mice were restored to levels that were
536 comparable to those of *Pou4f3-CreER*$^{+/-}$*Lphn2*$^{+/+}$ mice (Figures 11A-11C). Moreover, the
537 DPOAE thresholds of the *Lphn2*-deficient mice were also restored to nearly normal levels after
538 AAV-ie-*Lphn2pr*-LPHN2 treatment (Figure 11D). In contrast, *Lphn2*-deficient mice that were
539 treated with AAV-ie-*Lphn2pr*-mCherry showed no significant improvements in any of the

540 parameters mentioned above (Figures 11A-11D). The MET characteristics of LPHN2-
541 expressing cochlear hair cells in response to fluid jet stimulation were also evaluated. Our
542 results indicated that mCherry-labeled cochlear hair cells in AAV-ie-*Lphn2pr*-LPHN2-treated
543 *Pou4f3-CreER*$^{+/-}$*Lphn2*$^{fl/fl}$ mice showed MET currents with similar amplitudes and
544 responsiveness to D11 as those that were recorded for LPHN2-expressing hair cells in WT
545 cochleae (Figure 11E). In contrast, the severe impairments in the MET currents of LPHN2-
546 expressing cochlear hair cells from *Pou4f3-CreER*$^{+/-}$*Lphn2*$^{fl/fl}$ mice were not significantly
547 ameliorated by treatment with the AAV-ie-*Lphn2pr*-mCherry control virus (Figure 11E).
548 Collectively, these findings suggest that LPHN2 in cochlear hair cells directly contributes to
549 auditory perception through the sensation of mechanical force.
550

551 **Discussion**

552 Cochlear hair cells convert sound stimuli into electrochemical signals through the activation
553 of MET channels. A series of candidate components of the MET channel complex have been
554 identified, among which TMC1/2 were proposed to be pore-forming subunits (Jia et al., 2020;
555 Pan et al., 2018; Qiu and Muller, 2022). Because of the rapid activation and ultralow response
556 latency of cochlear hair cells in the submillisecond range, the MET process is conventionally
557 believed to be directly regulated by ion channels but not by GPCRs, which usually transduce
558 signals through second messengers or enzymatic pathways (Corey and Hudspeth, 1979;
559 Hudspeth, 2014). In the present work, we showed that a mechanosensitive GPCR, LPHN2,
560 actively participates in the MET process in cochlear hair cells. Notably, LPHN2 is distributed
561 at the tips of shorter rows of stereocilia in cochlear hair cells, where it colocalizes with MET
562 channel components. In contrast to the signaling mechanism for smell or visual perception,
563 which mainly relies on the secondary messenger system downstream of sensory GPCRs,
564 LPHN2 directly interacts with TMC1 and plays an important modulatory role in the MET
565 process during auditory perception; this conclusion was supported by genetic studies using
566 *Lphn2*-deficient mice, pharmacological studies using a specific LPHN2 inhibitor and single-
567 channel analyses in a heterologous reconstitution system. Importantly, our data suggested that
568 the sensation of force by LPHN2 was converted to conformational changes in TMC1,
569 increasing the probability of TMC1 opening. These data provide experimental evidence that a

570 mechanosensitive GPCR might be a component of the MET complex. Interestingly, the
571 *Drosophila* LPHN homolog, Ca^{2+}-independent receptor of latrotoxin (drCirl), has been reported
572 to respond to mechanical stimuli in vivo by interacting with the Toll-like receptor Tollo, which
573 modulates the sensitivity of *Drosophila* to tactile and auditory stimuli (Scholz et al., 2023;
574 Scholz et al., 2015). However, in contrast to the mechanism underlying the function of LPHN2
575 in mouse cochlear hair cells, Cirl converts mechanical stimulation to decrease the intracellular
576 cAMP levels in the sensory neurons of *Drosophila* (Scholz et al., 2017). Whether drCirl directly
577 couples to the *Drosophila* TMC homolog is worthy of future study. In addition, our parallel
578 study indicated that another LPHN subfamily members, namely LPHN3, can also be activated
579 in response to force stimulation, but heterozygous deficiency of this receptor resulted in no
580 obvious balance or hearing disorder phenotype (unpublished observation). Therefore, we
581 hypothesized that mechanosensitive LPHNs and their homologs might represent one subfamily
582 of evolutionally conserved auditory sensors. Whether mechanistic differences contributed to
583 faster and more accurate responses through evolutionary adaptation to sound stimuli in more
584 complex environments requires further investigation.

585 Frequency, amplitude and period are the three most important variables of sound. Other
586 variables may include timbre and envelope. In addition to hearing responses with very quick
587 latency that are mediated by MET (required for frequency detection), signals ranging from 20
588 to 500 ms may also contribute to hearing experiences (may contribute to period detection). For
589 example, our language communications do not always require very fast
590 sensation/differentiation. People normally differentiate speech with similar voice frequencies
591 at a rate of up to 9 syllables/second, indicating an approximately 110 ms differentiation time
592 (Coupe et al., 2019; Peelle and Davis, 2012). Moreover, the calcium influx that occurs in hair
593 cells in response to bundle deflection, which is a classic method for mimicking sound sensation
594 ex vivo, can last approximately 200 ms (Beurg et al., 2009). Hearing responses with a latency
595 of approximately 100 ms may play a regulatory role in responses to bundle deflection. These
596 findings raised the interesting possibility that not only force sensors with a response latency in
597 the microsecond range but also force sensors with a response latency ranging from 20 ms to
598 500 ms, as exemplified by GPCR-secondary messenger systems, could function as auditory
599 modulators that regulate neurotransmitter release and hearing sensations. Here, in addition to

its direct association with TMC1, our data suggested that LPHN2 activated Gs signaling and increased intracellular cAMP concentrations in cochlear hair cells in response to force stimulation. Previous studies suggested that cAMP signaling regulates the mechanotransduction process in rat cochlear hair cells and affects auditory sensitivity by regulating gating spring stiffness (Caprara and Peng, 2022; Mecca et al., 2022). Moreover, a loss-of-function mutation in adenylyl cyclase 1 (AC1), which is the upstream regulator of cAMP production, caused by the deletion of the 82 C-terminal amino acids has been associated with hearing loss in humans (Santos-Cortez et al., 2014). Therefore, Gs-cAMP signaling might also participate in auditory perception. However, our present work revealed that genetic ablation or pharmacological inhibition of Gs had no significant effect on the baseline MET of LPHN2-expressing hair cells or on their response to an LPHN2-specific inhibitor; these results suggest the dispensable role of Gs-cAMP signaling in the LPHN2-mediated regulation of MET. This result might be explained by the longer latency time of cAMP production (millisecond range) than that of acute MET (microsecond range). Nevertheless, we cannot exclude the possibility that force-induced Gs-cAMP signaling downstream of LPHN2 might also affect auditory perception by fine-tuning the sensitivity or adaptation of the MET process or by participating in longer-term regulation of hair cell physiology, such as neurotransmitter release or intercellular communication, via the regulation of cAMP-gated cation channel activity, such as CNG or HCN activity. Indeed, we have revealed an association between LPHN2 and CNGA3 in cochlear hair cells. Future studies using hair cell-specific Gs- or CNGA3-knockout mice combined with detailed activation/adaptation analyses of MET currents and neurotransmitter probing will be helpful for elucidating the functional roles of LPHN2-Gs-cAMP signaling in auditory perception.

We performed experiments to analyze the MET responses of cochlear hair cells expressing LPHN2 and that used the LPHN2 inhibitor D11, and our data suggested that auditory hair cells are heterogeneous in terms of force-sensitive GPCRs, such as LPHN2. Lphn2 was expressed in 80% of cochlear hair cells, and Lphn2 deficiency, specifically in *Pou4f3-CreER*$^{+/-}$*Lphn2*$^{fl/fl}$ mice, caused hearing loss but not complete hearing loss. These results suggested that both Lphn2-positive and Lphn2-negative hair cells play important roles in hearing processes but that these hair cells are not functionally redundant. Specifically, although Lphn2-deficient hair cells

630 exhibited severely impaired MET responses compared with those of control cells, LPHN2-
631 negative hair cells in WT cochleae generally exhibited MET currents that were comparable to
632 those of LPHN-positive hair cells (Figure S6C). Therefore, it is possible that other
633 mechanosensitive components might exist in LPHN2-negative hair cells to compensate for the
634 function of LPHN2 and regulate the MET response. There are many kinds of force, such as
635 tension force, normal force, and friction force, which further include static friction force, sliding
636 friction force, rolling friction force and fluid friction force. We indeed identified several force-
637 sensing GPCRs other than LPHN2, which exhibit different expression patterns from those of
638 LPHN2 in cochlear hair cells and also participate in the MET process (unpublished observation).
639 At least one of these mechanosensitive GPCRs (msGPCR2) expressed on stereocilia was able
640 to couple to TMC1. Similar to LPHN2, knockout or pharmacological inhibition of this
641 msGPCR2 decreased MET in fluid jet assay. These observations may account for the less severe
642 hearing loss phenotype observed in LPHN2-deficient mice compared with those with
643 deficiency for other MET components, such as CIB2 or TMIE (data will be presented in another
644 work)(Giese et al., 2017; Zhao et al., 2014). Currently, we do not know why hair cells need
645 multiple GPCRs to sense mechanical stimuli. We hypothesized that these GPCRs might be
646 sensitive to different mechanical stimuli in the cochlea or that these GPCRs might recognize
647 different variables of sound, such as frequency, amplitude and period. However, further studies
648 are needed to elucidate the detailed functions of these mechanosensitive GPCRs and to explore
649 the potential effects of their combinations on auditory perception. Moreover, from a single-cell
650 perspective, even the Lphn2^{+}Tmc1^{+}Gs^{+} cells exhibited heterogeneous MET responses to D11
651 treatment (approximately 30% of these cells were insensitive to D11), suggesting additional
652 layers of complexity in hair cell heterogeneity (Figure 6C). This is potentially consistent with
653 previous observations that SGNs driven by different cochlear hair cells could have different
654 firing rates (Sun et al., 2018).

655 Considering the four criteria that we have proposed to fulfil the auditory receptor
656 candidates, we found that Lphn2 is expressed in the stereocilia of cochlear hair cells (1); Lphn2
657 senses force with an EC50 of 1.7 ± 0.3 pN, which is within a physiological range (2~100
658 dynes/cm^{2}) (2); LPHN2 can convert force stimuli into membrane excitability by coupling to
659 TMC1 and eliciting neurotransmitter glutamate release (3); and finally, specifically knocking

660 out Lphn2 in hair cells causes hearing loss in mice (4). Therefore, our results suggest that
661 GPCRs, such as LPHN2, could be auditory receptor candidates.
662
663 **Limitations of the Study**
664 In this study, we have revealed an indispensable role of LPHN2 in auditory perception.
665 However, it remains unclear whether LPHN2 mutations are correlated with auditory defects.
666 Therefore, it will be important to revisit the potential pathogenetic roles of LPHN2 mutations
667 in hearing loss through genome-wide association meta-analysis and exome sequencing. Despite
668 our results indicating that the force applied on LPHN2 through LPHN-M-beads stimulates Ca^{2+}
669 responses and glutamate release in hair cells *ex vivo*, further studies are warranted to investigate
670 whether and how LPHN2 in cochlear hair cells converts the natural auditory stimuli into
671 intracellular chemical signals and neurotransmitter release. Although the magnetic-bead-
672 delivered force is theoretically within the physiological range, the relatively low binding
673 efficiency of the beads with endogenous LPHN2, as well as the potential time delay in
674 transmitting force, obscure its physiological significance. To this end, the force stimulus
675 delivered by a fluid jet or stiff probe, which mimics the natural mechanical stimulation on hair
676 cells, is required in future studies to determine the roles of LPHN2-mediated force sensation in
677 Ca^{2+} response or neurotransmitter release. Finally, our current results suggest a physical and
678 functional coupling between LPHN2 and TMC1. However, much remains unclear about the
679 interaction mode between these two multi-transmembrane proteins as well as the potential
680 relationship between the LPHN2-mediated TMC1 activation and tip link-mediated TMC1
681 activation. Further in-depth investigation using cryo-electron microscopy, or *in situ* cryo-
682 electron tomography, combined with molecular dynamic simulations will shed light on the
683 detailed structural information, which is expected to provide potential modulatory strategies for
684 treating auditory defects by targeting LPHN2.
685
686 **Data availability**
687 All data are available upon reasonable request from the corresponding authors.
688
689 **Acknowledgments**

This work was supported by National Key R&D Program of China (2019YFA0904200 to J.-P.S., 2023YFA1801100 to Z.Y.), National Science Fund for Distinguished Young Scholars Grant (81825022 to J.-P.S., 82225011 to X.Y.), National Natural Science Foundation of China (32130055 and 82330118 to J.-P.S., 82330022 to X.Y., 81770407 to C.W., 82271176 to W.-W.L.), the Key Research Project of the Beijing Natural Science Foundation, China (Z200019 to J.-P.S.), Major Fundamental Research Program of Natural Science Foundation of Shandong Province, China (ZR2020ZD39 to J.-P.S. Z.-G.X, and W.-W.L, ZR2021ZD18 to X.Y.), Shandong Provincial Natural Science Fund (ZR2023QH394 to M.-W.W.), Taishan Scholars Program of Shandong Province (tsqn201909189 to W.-W.L.), Key Project of Precision Medicine Joint Fund of Natural Science Foundation of Hebei Province (81770407 H2020206409 to C.W.) and the Cutting Edge Development Fund of Advanced Medical Research Institute (to Z.Y. , K.-K.Z. and J.-P.S.). J.-P.S. was also supported by the Tencent New Cornerstone Investigator Program.

Author contributions

J.-P.S. and X.Y. initiated, designed and supervised the overall project. J.-P.S. conceived the idea of searching for MET-regulating GPCRs in the cochlear system at 2011 and initiated the screening process by collaborating with Z.-G.X.. X.Y., C.W. and W.X. designed and supervised all electrophysiology experiments. Z.-G.X and R.-J.C. provided guidance and suggestions on the cochlear studies. Z.Y. and J.-P.S. developed the magnetic force stimulation assay to examine the activation of G proteins and second messengers downstream of GPCRs. Z.Y., M.-W.W., S.-H.Z. and Z.-C.S. performed the cell-based assay of LPHNs. Z.Y., Z.-C.S., S.-H.Z., Q.-Y.Z., J.-R.G. and Y.-Q.W. performed the electrophysiological experiments supervised by J.-P.S. and X.Y.. Z.Y., M.-W.W., S.-H.Z., Z.-C.S., Q.-Y.Z. and X.-H.W. performed the Ca^{2+} imaging. J.-P.S., Z.Y., M.-W.W. and S.-H.Z. participated in the design of gene knockout mice and modified AAV-ie. Z.Y., M.-W.W., Z.-C.S., Q.-Y.Z., W.-W.L. and L.X. performed cochlear behaviour studies. Z.Y., M.-W.W., Z.-C.S. and X.-H.W isolated mouse cochlea and performed immunofluorescence studies and ex vivo experiments. M.-W.W., S.-H.Z and Z.-C.S. performed single cell qRT-PCR. M.-W.W. and Y. G. performed coimmunoprecipitation and western blotting analyses. Z.Y. and Y.G. performed BRET experiments. Z.Y., M.-W.W., S.-H.Z., Z.-C.S.,

720 J.-R.G. and W.-W.L. performed the AAV-ie-related experiments. K.-K.Z. and X.W. performed
721 virtual screening and cellular assays under the supervision of J.-P.S. and X.Y.. J.-P.S., X.Y., Z.-
722 G.X, C.W., R.-J.C, Z.Y., M.-W.W., S.-H.Z. and Z.-C.S. participated in data analysis and
723 interpretation. Z.-G.X., C.W., W.X., W.-W.L. and L.X. provided insightful ideas related to the
724 auditory sensation. Z.Y., M.-W.W., S.-H.Z., Z.-C.S., K-.K.Z, X.W., Q.-Y.Z., Y.G. and J.-R.G.
725 prepared the figures. J.-P.S., X.Y., Z.Y., Z.-G.X and C.W. wrote the manuscript. All the authors
726 have seen and commented on the manuscript.
727
728 **Competing interests**
729 The authors declare no competing interests.
730
731 **Figure legends**
732 **Figure 1. Expression of LPHN2 in cochlear hair cells**
733 **(A)** mRNA levels of *Lphn2* in the cochlear epithelium isolated from WT mice at E20, P1, P7,
734 P14, P30, P60, P120 and P240 (n = 6). Data are normalized to the mRNA levels of *Lphn2* at
735 E20. E, embryonic period; P, postnatal day.
736 **(B)** Immunostaining (left) and quantitative analysis (right) of LPHN2 expression in hair cells
737 from different sections of cochlear whole mounts derived from WT mice at P10 (n = 3 mice per
738 group). Scale bar, 20 μm.
739 **(C)** Representative blotting showing the protein levels of LPHN2 in the stereocilia and cell
740 body of cochlear or utricle hair cells isolated from WT mice at P10. Representative blotting
741 from three independent experiments are shown (n = 3). LPHN2 antibody against the N terminus
742 (551 - 600 residues) was used, which revealed both the full-length (~130 kDa) and the N-
743 terminal fragment of LPHN2 (~120 kDa) in the cochlear or utricle hair cells. Data are correlated
744 to Figure S1F-S1G.
745 **(D)** Schematic diagram showing the expression pattern of LPHN2 in cochlear and utricle hair
746 cells, respectively.
747 **(E)** Co-immunostaining of LPHN2 (green) and Phalloidin (magenta) in the stereocilia of OHC
748 top) and IHC (bottom) in cochlear whole mounts derived from WT mice at P10 (n = 6 mice per
749 group). Scale bar, 5 μm. White arrows show the localization of LPHN2 at the tips of shorter

750 rows of stereocilia. Data are correlated to Figure S1H.

751 **(F)** Co-immunostaining of LPHN2 (green) and Myosin7a (magenta) in cochlear sections
752 derived from WT mice at P30 (n = 6 mice per group). Scale bar, 20 μm. White arrows show the
753 distribution of LPHN2 above the apical surface of hair cells.

754 **(G)** Expression of LPHN2-mCherry (magenta) in the stereocilia of IHC in cochlear whole
755 mounts derived from WT or LPHN2^{mCherry} mice at P10 (n = 6 mice per group). Scale bar, 5 μm.
756 White arrows show the localization of LPHN2 at the tips of shorter rows of stereocilia. Data
757 are correlated to Figure S1I-S1J.

758

759 **(A)** *P < 0.05; ***P < 0.001. WT mice at postnatal time points compared with those at E20. **(B)**
760 ns, no significant difference. Hair cells at middle or basal turn compared with those at apical
761 turn. The bars indicate mean ± SEM values. All data were statistically analyzed using one-way
762 ANOVA with Dunnett's post hoc test.

763

764 **Figure 2. LPHN2 deficiency severely impairs hearing**

765 **(A-D)** ABR thresholds (A), ABR waveforms at click (B), ABR peak1 (P1) latency (left) and
766 amplitude (right) (C), and DPOAE thresholds (D) of *Pou4f3-CreER*$^{+/-}$*Lphn2*$^{+/+}$ (referred to as
767 *Pc-Lphn2*$^{+/+}$) and *Pou4f3-CreER*$^{+/-}$*Lphn2*$^{fl/fl}$ (referred to as *Pc-Lphn2*$^{fl/fl}$) mice at P30 (n = 8 mice
768 per group).

769 **(E)** Immunostaining of Myosin7a (red) in cochlear hair cells derived from *Pc-Lphn2*$^{+/+}$ and *Pc-*
770 *Lphn2*$^{fl/fl}$ mice at P30 (n = 6 mice per group). Scale bar, 20 μm. Data are correlated to Figure
771 S2O.

772 **(F)** Left: Representative SEM images showing hair bundle morphology of the OHC and IHC
773 from *Pc-Lphn2*$^{+/+}$ and *Pc-Lphn2*$^{fl/fl}$ mice at P30. Scale bar, 1 μm (OHC) or 2 μm (IHC). Right:
774 Quantitative analysis of the width index of hair bundles of the OHC from *Pc-Lphn2*$^{+/+}$ and *Pc-*
775 *Lphn2*$^{fl/fl}$ mice at P30 (n = 6 mice per group).

776 **(G)** Co-immunostaining of Phalloidin (magenta) and different MET machinery components
777 (green), including TMC1, TMC2, PCDH15, CDH23, TMIE and LHFPL5, in cochlear hair cells
778 of *Pc-Lphn2*$^{fl/fl}$ and *Pc-Lphn2*$^{+/+}$ mice (n = 6 mice per group).

779

780 **(A, C-D, F)** **P < 0.01; ***P < 0.001; ns, no significant difference. *Pc-Lphn2*$^{fl/fl}$ mice compared
781 with *Pc-Lphn2*$^{+/+}$ mice. The bars indicate mean ± SEM values. All data were statistically
782 analyzed using two-way ANOVA with Dunnett's post hoc test (A, D) or unpaired two-sided
783 student's *t* test (C, F).
784
785 **Figure 3. Force sensation by LPHN2 induces endogenous cAMP production**
786 **(A)** Schematic representation of the force-induced LPHN2 activation in HEK293 cells using a
787 magnetic system.
788 **(B)** Dose-dependent cAMP accumulation in HEK293 cells transfected with plasmid encoding
789 LPHN2 in response to force applied via LPHN2-M-beads or polylysine-coated Ctrl-beads (n =
790 3). Data are correlated to Figure S3C.
791 **(C)** Endogenous cAMP level changes in the cochlea (apex, middle or base) and utricle explant
792 derived from *Pc-Lphn2*$^{+/+}$ or *Pc-Lphn2*$^{fl/fl}$ mice at P10 in response to force (3 pN) applied by
793 LPHN2-M-beads in the absence or presence of NF449 (20 μM) (n = 6). Data are correlated to
794 Figure S3D.
795 **(D)** mRNA levels of different G protein subtypes in LPHN2-expressing cochlear hair cells
796 derived from P10 mice measured by single-cell qRT-PCR (n = 20 hair cells). The mRNA levels
797 of respective G protein subtypes in the brain were used as the reference (normalized to 1).
798
799 **Figure 4. LPHN2 deficiency impairs MET currents**
800 **(A)** Schematic illustration of the labelling of LPHN2-expressing hair cells by AAV-ie-*Lphn2pr*-
801 mCherry (referred to as AAV-ie-*L2pr*-mCherry) and the MET current recording by fluid-jet
802 stimulation. Data are correlated to Figure S4A-S4B.
803 **(B)** Representative MET current traces induced by sinusoidal fluid-jet stimulation in cochlear
804 OHCs (top) and IHCs (bottom) of *Pc-Lphn2*$^{+/+}$ mice (red) or *Pc-Lphn2*$^{fl/fl}$ mice (blue) at P10.
805 **(C)** Quantification of the saturated MET currents in cochlear OHCs and IHC of *Pc-Lphn2*$^{+/+}$
806 mice or *Pc-Lphn2*$^{fl/fl}$ mice at P10 (n = 12 for OHCs and n = 14 for IHCs).
807
808 **(C)** ***P < 0.001; *Pc-Lphn2*$^{+/+}$ mice compared with *Pc-Lphn2*$^{fl/fl}$ mice. The bars indicate mean
809 ± SEM values. All data were statistically analysed using unpaired two-sided Student's *t* test.

810

811 **Figure 5. Identification of selective LPHN2 inhibitor antagonizing its force sensation**

812 **(A)** Simulated inactive LPHN2-β structural model according to the cryo-EM structure of the
813 inactive CD97 (PDB: 8IKJ). The LPHN2-specific pocket residues that are not conserved among
814 aGPCRs are shown.

815 **(B)** The procedures for in-silico screening of selective LPHN2 inhibitors. 100 million
816 compounds were virtually screened against the putative orthosteric pocket of LPHN2 and the
817 top 5000 were selected for the second round of screening against the LPHN2-specific pocket
818 residues. The resultant top 300 molecules were subjected to clustering analysis, leading to 48
819 candidates. The final hit was identified by *in vitro* BRET-based G protein dissociation assay.

820 **(C)** Heatmap showing the inhibitory effects of the 48 candidate molecules on the force (3 pN)-
821 induced Gs activation in LPHN2-overexpressing HEK293 cells measured by BRET-based G
822 protein dissociation assay. Data are from 3 independent experiments (n = 3).

823 **(D)** Dose-dependent inhibition of D11 on the force (3 pN)-induced Gs activation in LPHN2-
824 overexpressing HEK293 cells (n = 3).

825 **(E)** The chemical structure of the LPHN2 inhibitor D11.

826 **(F-G)** The binding pose of D11 in the ligand pocket of LPHN2 (F) and the detailed interactions
827 between D11 and LPHN2 pocket residues (G) according to computational simulation.

828 **(H)** Effects of alanine mutation of LPHN2 pocket residues on the inhibitory potency of D11.
829 The heatmap was generated according to the differences of inhibitory potency (ΔpEC50) of
830 D11 between wild-type LPHN2 and its mutants. Data are from 3 independent experiments (n =
831 3). ND, no detectable inhibition.

832 **(I)** Inhibitory effects of D11 on force (3 pN)-induced or ligand-induced G protein activation in
833 HEK293 cells transfected with distinct combinations of aGPCR and G protein probes. Data are
834 from 3 independent experiments (n = 3).

835

836 **Figure 6. LPHN2 regulates MET currents in TMC1-dependent and Gs-independent**
837 **manner**

838 **(A)** schematic representation (upper panel) and quantitative analysis (bottom panel) of cochlear
839 hair cell subclasses according to the expression of *Lphn2*, *Tmc1*, and *Gnas*. Data are correlated

840 to Figure 6B-6C.

841 **(B-C)** Representative current traces (B) and quantitative analysis (C) of fluid jet-stimulated
842 MET responses of distinct cochlear hair cell subclasses pretreated with control vehicle or 50
843 nM D11. Data are normalized to the saturated MET response of control vehicle-treated hair
844 cells in respective subclasses (n = 14, 4, 35, and 22 for *Lphn2*$^{-}$*Tmc1*$^{+}$, *Lphn2*$^{+}$*Tmc1*$^{-}$,
845 *Lphn2*$^{+}$*Tmc1*$^{+}$*Gnas*$^{+}$ and *Lphn2*$^{+}$*Tmc1*$^{+}$*Gnas*$^{-}$ cells, respectively). Data are correlated to Figure
846 S6C.

847 **(D-E)** Representative current traces (D) and quantitative analysis (E) of fluid jet-stimulated
848 MET responses of cochlear hair cells derived from *Pc-Lphn2*$^{+/+}$, *Pc-Lphn2*$^{fl/fl}$, *Pc-Gnas*$^{+/+}$, or
849 *Pc-Gnas*$^{fl/fl}$ mice in the absence or presence of 50 nM D11 or 20 μM NF449. Data are
850 normalized to the saturated MET response of control vehicle-treated hair cells in respective
851 groups (n = 10, 15, 11, 11, 10 and 11 for *Pc-Lphn2*$^{+/+}$, *Pc-Lphn2*$^{fl/fl}$, *Tmc1*$^{-/-}$, *Pc-Gnas*$^{+/+}$, *Pc-*
852 *Gnas*$^{fl/fl}$ or NF449-treated *Pc-Gnas*$^{+/+}$ cells, respectively). Data are correlated to Figure S6F-
853 S6G.

854

855 **(C, E)** **P < 0.01; ***P < 0.001; ns, no significant difference. Cochlear hair cells pretreated
856 with D11 compared with those treated with control vehicle. The bars indicate mean ± SEM
857 values. All data were statistically analysed using paired two-sided Student's *t* test.

858

859 **Figure 7. LPHN2 colocalizes and associates with MET channel components**

860 **(A)** Schematic representation of the LPHN2-GAIN purification and mass spectrometry-based
861 proteomic strategies used to identify potential LPHN2 interacting proteins in mouse cochlea.

862 **(B)** Representative gel image showing the interacting proteins pulled-down by LPHN2-GAIN-
863 batis or control baits (empty anti-Flag M2 beads). Red arrow indicates the band with similar
864 molecular weight as TMC1.

865 **(C)** MET channel components (TMC1 and PCDH15) specifically detected in cochleae
866 homogenate pulled-down by LPHN2-GAIN-baits but not in that pulled-down by control baits.
867 Data are correlated to Table S2.

868 **(D)** Co-immunoprecipitation of LPHN2 with MET channel components (TMC1, PCDH15,
869 LHFPL5 and TMIE) in the lysates of mouse cochlea. Representative blotting from three

870 independent experiments is shown (n = 3).

871 **(E)** Co-immunostaining of LPHN2 (green) with MET channel components (magenta) in the
872 stereocilia of OHC in cochlear whole mounts derived from WT mice (n = 6 mice per group).
873 Scale bar, 5 μm. Arrows indicate the colocalization of LPHN2 with MET channel components
874 at the tips of shorter rows of stereocilia.

875 **(F)** Pearson's correlation analysis of the colocalization of LPHN2 with MET channel
876 components. The Pearson's correlation coefficient was 0.52, 0.53, 0.54 and 0.42 for the
877 colocalization of LPHN2 with TMC1, LHFPL5, PCDH15 and TMIE, respectively. Data are
878 correlated to Figure 7E.

879

880 **Figure 8. LPHN2 regulates MET through coupling to TMC1**

881 **(A)** Heatmap showing the efficiency of top 50 abundantly-expressed GPCRs in cochlear hair
882 cells for trafficking the TMC1 onto the plasma membrane. The efficiency was calculated as the
883 ratio of TMC1 immunofluorescence intensity on plasma membrane to that in cytosol in
884 HEK293 cells co-transfected with TMC1 and GPCR. Data are from 3 independent experiments
885 (n = 3).

886 **(B)** Left panel: Co-immunostaining of TMC1 (green) with GPCR-hc1 (magenta) in HEK293
887 cells transfected with TMC1 only or with TMC1 and GPCR-hc1. Scale bar: 20 μm.
888 Representative images from three independent experiments were shown (n = 3). Right panel:
889 Pearson's correlation analysis of TMC1 and GPCR-hc1 fluorescence intensities. The Pearson's
890 correlation coefficient was 0.62.

891 **(C)** Upper panel: Representative spontaneous single-channel currents of TMC1 at -40 mV
892 recorded in HEK293 cells transfected with only TMC1 or GPCR-hc1, or with TMC1 and
893 GPCR-hc1. Bottom panel: The normalized all-point amplitude histogram analysis of single-
894 channel currents in HEK293 cells transfected with TMC1 and GPCR-hc1. The distribution data
895 were fitted by a sum of two Gaussians, and the peaks correspond to the closed (C) and open (O)
896 states.

897 **(D)** Scatterplots of the single-channel open probability (Po) in HEK293 cells transfected with
898 only TMC1 or GPCR-hc1, or with TMC1 and GPCR-hc1 (n = 11 per group). Data are correlated
899 to Figure 8C.

900 **(E)** The current-voltage relationship of the spontaneous currents recorded in HEK293 cells
901 transfected with TMC1 and GPCR-hc1 (n = 3). The The single-channel conductance of TMC1
902 was determined as 82.3 ± 6.4 pS. Data are correlated to Figure S7E.
903 **(F-H)** Representative spontaneous and force (10 pN)-stimulated single-channel current traces
904 recorded in HEK293 cells transfected with TMC1 and GPCR-hc1 pretreated with control
905 vehicle (F), 10 μM NF449 (G), or 50 nM D11(H). Data are correlated to Figure 8I-8J.
906 **(I)** Histogram showing single-channel open probability at rest condition (black) and in response
907 to 10 pN force stimulation (red). Data are correlated to Figure 8F.
908 **(J)** Effect of NF449 or D11 treatment on the force-induced single-channel open probability (n
909 = 6, 3 and 3 for control vehicle, NF449 and D11 treated group, respectively). Data are correlated
910 to Figure 8F-8H.
911
912 (**D**) ***P < 0.001; ns, no significant difference. HEK293 cells transfected with TMC1 or GPCR-
913 hc1, or with TMC1 and GPCR-hc1 compared with the control cells. (**J**) *p < 0.05; **P < 0.01.
914 Force-stimulated cells compared with control cells. ns, no significant difference. NF449-treated
915 cells compared with control vehicle-treated cells. The bars indicate mean ± SEM values. All
916 data were statistically analyzed using one-way (D) or two-way (J) ANOVA with Dunnett's post
917 hoc test.
918
919 **Figure 9. LPHN2 converts force stimuli into the conformational change of TMC1**
920 **(A)** Schematic diagram showing the generation of BRET pairs by fusing YFP at the N- or C-
921 terminus of TMC1 (referred to as N-YFP-TMC1 or C-YFP-TMC1) and inserting Nluc into
922 specific positions of different ICLs of LPHN2 (referred to as L2-ICL1-Nluc, L2-ICL2-Nluc,
923 L2-ICL3-Nluc and L2-Cter-Nluc, respectively).
924 **(B)** Saturation BRET signals between NLuc and YFP in HEK293 cells co-transfected with a
925 fixed amount of NLuc-tagged LPHN2 and an increasing amount of TMC1-YFP. Data are from
926 three independent experiments (n = 3). Data are correlated to Figure S8A.
927 **(C)** Interaction model of LPHN2 and TMC1 according to computational simulation.
928 (D) Force-induced intermolecular BRET signals between C-YFP-TMC1 and Nluc-tagged
929 LPHN2 (n = 4).

930 **(E)** Force-induced dose-dependent BRET signal increase between C-YFP-TMC1 and Nluc-
931 tagged LPHN2 (n = 3).
932 **(F)** Schematic diagram showing the generation of TMC1 conformational sensors by fusing the
933 Nluc at the N-terminus of TMC1 and inserting the FlAsH probes (CCPGCC) into specific
934 positions of different ICLs of TMC1.
935 **(G)** Intramolecular BRET signals between the Nluc and FlAsH probes in the respective Nluc-
936 TMC1-FlAsH constructs in response to the force stimulation on LPHN2 (n = 4). Data are
937 correlated to Figure S8B.
938 **(H)** Intramolecular BRET signals between the Nluc fused in ICL4 of TMC1 and FlAsH probes
939 inserted at ICL2 or ICL3 in response to the force stimulation on LPHN2 (n = 4). Data are
940 correlated to Figure S8C.
941 **(I)** Schematic diagram showing the movement of ICL2/3 and ICL4 or TMC1 towards the
942 opposite direction in response to force stimulation on LPHN2.
943 **(J)** Effects of pretreatment with si*GNAS*, NF449 (10 μM) or D11 (50 nM) on the force-induced
944 intramolecular BRET signals between the Nluc fused in ICL4 of TMC1 and FlAsH probes
945 inserted at ICL2 or ICL3 (n = 4).
946
947 (**D, G, H**) *P < 0.05; **P < 0.01; ***P < 0.001; ns, no significant difference. Force-stimulated
948 HEK293 cells compared with the control cells. **(J)** ***P < 0.001; ns, no significant difference.
949 HEK293 cells treated with si*GNAS*, NF449 or D11 compared with those treated with control
950 siRNA or control vehicle. The bars indicate mean ± SEM values. All data were statistically
951 analyzed using unpaired two-sided Student's *t* test (D, G, H) or one-way ANOVA with
952 Dunnett's post hoc test (J).
953
954 **Figure 10. Force sensation by LPHN2 induces glutamate release and Ca^{2+} signals in**
955 **cochlear hair cells**
956 **(A)** Schematic diagram showing the working mechanism of the red fluorescent glutamate
957 sensor Rncp-iGluSnFR (Rncp-iGlu).
958 **(B-C)** Representative traces (B) and quantitative analysis (C) of glutamate secretion from
959 individual cochlear hair cell derived from the P10 *Pc-Lphn2*$^{+/+}$ mice in response to force

applied by LPHN2-M-beads or control beads (n = 9). Data are correlated to Figure S9A-S9B.

(D) Force-induced dose-dependent glutamate secretion from cochlear hair cells in the absence or presence of D11. Representative curves from three independent experiments are shown (n = 3).

(E) Schematic illustration of the Ca^{2+} imaging in mouse cochlea hair cells labelled by AAV-ie-*L2pr*-mCherry in response to force stimulation.

(F) Heatmaps showing the Ca^{2+} responses in individual cochlear hair cell derived from the P10 *Pc-Lphn2*$^{+/+}$ or *Pc-Lphn2*$^{fl/fl}$ mice. n=60 for the AAV-ie-*L2pr*-mCherry-labelled cochlear hair cells from *Pc-Lphn2*$^{+/+}$ mice (yellow frame); n=10 for the unlabelled hair cells from *Pc-Lphn2*$^{+/+}$ mice (orange frame); n = 20 for the AAV-ie-*L2pr*-mCherry-labelled cochlear hair cells from *Pc-Lphn2*$^{fl/fl}$ mice (green frame). Y axis represents the magnitude of the calcium response characterized by $\triangle F/F_0$.

(G) Representative Ca^{2+} traces recorded in individual cochlear hair cells derived from P10 *Pc-Lphn2*$^{+/+}$ or *Pc-Lphn2*$^{fl/fl}$ mice.

(H) Dose-dependent inhibitory effects of D11 treatment on force-stimulated Ca^{2+} responses in cochlear hair cells labelled by AAV-ie-*L2pr*-mCherry. Data are correlated to Figure S9C.

(C) ***$P < 0.001$. Cochlea explants treated with LPHN2-M-beads compared with those treated with Ctrl-beads. The bars indicate mean ± SEM values. Data were statistically analyzed using unpaired two-sided Student's *t* test.

Figure 11. LPHN2 re-expression in cochlear hair cells of Lphn2-deficient mice rescues hearing loss and MET

(A-D) ABR thresholds (A), ABR peak1 (P1) latency (B) and amplitude (C), and DPOAE thresholds (D) of *Pc-Lphn2*$^{+/+}$, *Pc-Lphn2*$^{fl/fl}$, AAV-ie-*L2pr*-LPHN2-treated *Pc-Lphn2*$^{fl/fl}$ mice (referred to as AAV-ie-*L2pr*-LPHN2 mice) and AAV-ie-*L2pr*-mCherry-treated *Pc-Lphn2*$^{fl/fl}$ mice (referred to as AAV-ie-*L2pr*-mCherry mice) at P30 (n = 6 mice per group). Data are correlated to Figure S7A-S7E.

(E) Representative current traces (left) and quantitative analysis (right) of fluid jet-stimulated MET responses of cochlear hair cells derived from *Pc-Lphn2*$^{+/+}$, AAV-ie-*L2pr*-LPHN2 or AAV-

990 ie-*L2pr*-mCherrymice in the absence or presence of 50 nM D11 (n = 9, 14 and 10 for *Pc-*
991 *Lphn2*$^{+/+}$, AAV-ie-*L2pr*-LPHN2 or AAV-ie-*L2pr*-mCherry cells, respectively).
992
993 **(A-D)** **P < 0.01; ***P < 0.001; ns, no significant difference. *Pc-Lphn2*$^{fl/fl}$, AAV-ie-*L2pr-*
994 LPHN2 or AAV-ie-*L2pr*-mCherry mice compared with *Pc-Lphn2*$^{+/+}$ mice. **(E)** **P < 0.01; ns,
995 no significant difference. Cochlea explants treated with D11 compared with those treated with
996 control vehicle. The bars indicate mean ± SEM values. All data were statistically analyzed using
997 one-way ANOVA with Dunnett's post hoc test (A-D) or paired two-sided Student's *t* test (E).
998
999 **Methods**
1000 **Mice**
1001 C57BL/6J wild-type mice were obtained from Jackson Laboratory. *Lphn2*$^{+/-}$ (S-KO-15867),
1002 *Lphn2*$^{fl/fl}$ (S-CKO-17378), *Tmc1*$^{-/-}$ mice (S-KO-18952), *Gnas*$^{fl/fl}$ and LPHN2^{mCherry} mice with
1003 C57BL/6J background were purchased from Cyagen (Suzhou, China). *Pou4f3-CreER* mice
1004 with C57BL/6J background were generated by GemPharmatech (Nanjing, China). The *Pou4f3-*
1005 *CreER* line was generated by placing the *CreERT2* element downstream of the endogenous
1006 coding sequence of Pou4f3, which were separated by a P2A sequence. The *Pou4f3-CreER*$^{+/-}$
1007 *Lphn2*$^{fl/fl}$ and *Pou4f3-CreER*$^{+/-}$*Gnas*$^{fl/fl}$ mice were generated by crossing *Pou4f3-CreER*$^{+/-}$ mice
1008 with *Lphn2*$^{fl/fl}$ mice and *Gnas*$^{fl/fl}$ mice, respectively. For activation of Cre recombinase in
1009 *Pou4f3-CreER*$^{+/-}$ mice, the mice were treated with tamoxifen (75 mg/kg) dissolved in corn oil
1010 through round window membrane (RWM) injection at P25 (left ear) and P26 (right ear)
1011 consecutively. For activation of Cre recombinase in *Pou4f3-CreER*$^{+/-}$ mouse embryos, the
1012 pregnant mice at 14 days post coitum (E14) was treated with 100 mg/kg tamoxifen
1013 supplemented with 37.5 mg/kg progesterone for 3 consecutive days through *i.p.* injection. All
1014 mice were housed at Shandong University Animals Care Facility, with a 12 hr light/12 hr dark
1015 cycle and ad libitum access to water. Both male and female mice were used and were randomly
1016 assigned to experimental groups. All mice care and experiments were reviewed and approved
1017 by Animal Use Committee of Shandong University Cheeloo College of Medicine.
1018
1019 **Cell lines**

1020 Human embryonic kidney 293 (HEK293) cells were obtained from American Type Culture
1021 Collection (ATCC, Manassas, VA, USA) and were cultured in DMEM supplemented with 10
1022 % fetal bovine serum, penicillin (100 IU/ml), and streptomycin (100 mg/ml) in 5 % CO_2 at 37
1023 °C. Cell transfection was performed with Lipofectamine 2000 (Invitrogen) according to the
1024 manufacturer's instructions.
1025

1026 **RNA extraction and Quantitative reverse-transcriptase PCR**

1027 Total RNA was extracted from the brain or cochlear epithelium of WT mice using TRIzol
1028 reagent (Invitrogen). cDNA was synthesized using the qRT-PCR Kit (Toyobo, FSQ-101) and
1029 the quantitative reverse-transcriptase PCR (qRT-PCR) was conducted using FastStart SYBR
1030 Green Master (Roche) on a LightCycler qPCR system (Bio-Rad). The relative mRNA levels of
1031 target genes, including *Lphn2*, *Tmc1* and *Gnas* subtypes and G protein subtypes, were
1032 calculated using *Actb* as an internal control. For single cell qRT-PCR, RNA was extracted from
1033 single cochlear hair cell (or AAV-ie-*Lphn2pr*-mCherry-labeled cochlear hair cell) using
1034 Discover-sc® WTA Kit V2 (Vazyme, N711). The cDNA synthesis, qRT-PCR and data
1035 processing were performed as described above. The sequences of all the primers used in the
1036 present study are listed in Table S1.
1037

1038 **Stereocilia separation**

1039 The stereocilia was separated from the hair cell body using a modified twist-off method as
1040 described previously (Avenarius et al., 2017; Gillespie and Hudspeth, 1991). Briefly, circular
1041 coverslip sheet with a diameter of 14 mm was soaked with a 4% ammonium hydroxide and 4%
1042 hydrogen peroxide solution, washed with water, and soaked in methanol. The coverslip was air-
1043 dried and then coated with 1 μL Corning® Cell-Tak™ Cell and Tissue Adhesive. Dissected
1044 basilar membrane of mouse cochlea was dropped onto the coverslips in dissection media and
1045 gently pressed to the coverslip with the epithelium side down. The basilar membrane was then
1046 removed, and stereocilia samples that are stuck on the coverslip were immunostained by
1047 phalloidin or gently scraped off for further analysis.
1048

1049 **Western blotting**

1050 The brain, cochlea or utricle from WT, *Lphn2*$^{+/-}$, *Lphn2*$^{-/-}$, *Pou4f3-CreER*$^{+/-}$*Lphn2*$^{+/+}$ or
1051 *Pou4f3-CreER*$^{+/-}$*Lphn2*$^{fl/fl}$ mice, or the isolated stereocilia and cell bodies of cochlear hair cells,
1052 or HEK293 cells transfected with LPHNs or empty plasmid pcDNA3.1 were collected with
1053 NP40 lysis buffer containing phosphatase and protease inhibitors. After centrifugation at 12,000
1054 rpm for 20 min at 4 °C, the supernatant containing target proteins were collected. After
1055 determining the protein concentrations by BCA assay, the proteins were subjected to western
1056 blotting. Antibodies used in this study include anti-LPHN2 Rabbit antibody (Boster A30833,
1057 1:1000), anti-VLGR1 Goat antibody (Santa Cruz sc-21252, 1:1000), anti-Myosin7a Mouse
1058 antibody (DHSB 138-1, 1:1000), anti-PCDH15 Rabbit antibody (Biomatik CAU22931,
1059 1:1000), anti-CDH23 Mouse antibody (Santa cruz SC-166066, 1:1000), anti-FLAG Mouse
1060 antibody (Sigma F1804, 1:1000), anti-TMC1 Rabbit antibody (Abcam ab199949, 1:1000), anti-
1061 LHFPL5 Rabbit antibody (Thermo Fisher Scientific PA5-23919, 1:1000), anti-TMIE Rabbit
1062 antibody (Thermo Fisher Scientific PA5-58330, 1:1000), and anti-GAPDH Rabbit antibody
1063 (Abways AB0037, 1:10000).
1064
1065 **Immunofluorescence staining and confocal microscopy**
1066 For whole-mount immunostaining, the mouse temporal bones of WT, *Pou4f3-CreER*$^{+/-}$
1067 *Lphn2*$^{+/+}$, *Pou4f3-CreER*$^{+/-}$*Lphn2*$^{fl/fl}$, or the *Pou4f3-CreER*$^{+/-}$*Lphn2*$^{fl/fl}$ mice treated with AAV-
1068 ie-LPHN2 or AAV-ie-*Lphn2pr*-mCherry were fixed with 4% paraformaldehyde overnight at 4
1069 °C. The cochlea was dissected as whole and treated with 0.5 M EDTA for 3~5 h at 37 °C for
1070 decalcification. After three washing with PBS, the cochlea was permeabilized and blocked with
1071 PBS containing 0.5 % Triton-X and 5 % goat serum for 2 h. The cochlea whole mount was
1072 incubated with primary antibodies overnight at 4 °C, followed by incubation with secondary
1073 antibodies for 1~2 h at 37 °C. The samples were washed three times with PBS, mounted in
1074 ProLong Gold Antifade (Thermo Fisher Scientific, Waltham, MA), and subjected to
1075 fluorescence microscopic analysis using a LSM980 laser scanning confocal microscope system
1076 (ZEISS, Germany). Image acquisition and merging were performed using ZEISS Zen software.
1077 For the cryosection immunostaining, the decalcified cochlea was sequentially dehydrated
1078 using sucrose solution with concentration gradient (15 %, 20 % and 30 % in PBS). The cochlea
1079 was embedded in Tissue-Tek OCT compound (Sakura Fintek USA, Torrance, CA) and 6 μm

1080 sections were cut. The cochlea slices were incubated with blocking buffer at 37 °C for 2 h and
1081 were processed for immunostaining and fluorescence microscopic analysis.
1082 To investigate the subcellular localization of TMC1 in HEK293 cells, the cells were
1083 transiently transfected with plasmids encoding TMC1 and different GPCRs. 24 hours after
1084 transfection, the cells were seeded into 35-mm fibronectin-coated glass-bottom dish at the
1085 density of 5×10^5 cells/dish. After another 24 hours, the cells were fixed and processed for
1086 immunostaining and fluorescence microscopic analysis.
1087 Primary antibodies used in the present study were as follows: anti-LPHN2 Rabbit antibody
1088 (Sigma HPA043447, 1:200), anti-Myosin7a Mouse antibody (DHSB 138-1, 1:800), Phalloidin-
1089 iFluor 594 (Abcam ab176757, 1:5000), Phalloidin-iFluor 488 (Abcam ab176753, 1:5000),
1090 Phalloidin-iFluor 647 (Abcam ab176759, 1:5000), mouse anti-spectrin α (Sigma-Aldrich,
1091 ZRB2080, 1:100), anti-PCDH15 Rabbit antibody (Abcam ab202560, 1:100), anti-CDH23
1092 Mouse antibody (Santa cruz SC-166066, 1:100), anti-TMC1 Rabbit antibody (Merck ABN1649,
1093 1:100), anti-TMC2 Rabbit antibody (Abcam ab200039, 1:100), anti-LHFPL5 Rabbit antibody
1094 (Thermo Fisher Scientific PA5-23919, 1:100), anti-TMIE Rabbit antibody (Thermo Fisher
1095 Scientific PA5-58330, 1:100), and anti-FLAG Mouse antibody (Sigma F1804, 1:100).
1096 Secondary antibodies were as follows: Alexa Fluor Plus 555 Goat anti-Mouse IgG (Invitrogen,
1097 A32727), Alexa Fluor Plus 488 Goat anti-Rabbit IgG (Invitrogen, A32731) and Alexa Fluor
1098 Plus 647 Goat anti-Mouse IgG (Invitrogen, A32728).
1099

1100 **Auditory brainstem response (ABR) measurements**

1101 The *Lphn2*$^{+/-}$, *Pou4f3-CreER*$^{+/-}$*Lphn2*$^{fl/fl}$ mice or their wild-type littermates at P30, or the
1102 *Pou4f3-CreER*$^{+/-}$*Lphn2*$^{fl/fl}$ mice treated with AAV-ie-LPHN2 or control virus at P30 were placed
1103 on an isothermal pad to keep the body temperature at 37 °C during the experiment. After
1104 anesthetization with ketamine (100 mg/kg) and xylazine (25 mg/kg) intraperitoneally,
1105 electrodes were inserted subcutaneously at the vertex and pinna as well as near the tail. The
1106 stimulus generation, presentation, ABR acquisition, and data management were coordinated
1107 using an RZ6 workstation and BioSig software (Tucker Davis Technologies, Inc.). Acoustic
1108 stimuli (clicks or pure-tone bursts) of various sound levels were generated using high-frequency
1109 transducers. At each sound level, 512 responses were sampled and averaged. ABR thresholds

1110 were determined for each animal as the lowest sound level at which all ABR waves were
1111 detectable.
1112
1113 **Distortion product otoacoustic emission (DPOAE) measurements**
1114 Mice were anesthetized and maintained as described for ABR experiment. Two sine wave
1115 tones (f2 = 1.2 × f1) were presented for 1 sec durations at various sound levels. The emitted
1116 acoustic signal was then picked up by a microphone and digitized, and the magnitude of the
1117 distortion product (2 × f1-f2) was determined. The surrounding noise floor was calculated by
1118 averaging adjacent frequency bins around the frequency of the distortion product. DPOAE
1119 thresholds were determined as the lowest stimulus sound level at which the emitted signal of
1120 the distortion product was at least 5 dB SPL above the noise floor.
1121
1122 **Scanning Electron Microscopy (SEM)**
1123 Mouse temporal bones were fixed with 2.5 % glutaraldehyde in 0.1 M phosphate buffer
1124 overnight at 4 °C. Cochlea were dissected out of the temporal bone and post-fixed with 1 %
1125 osmium tetroxide in 0.1 M phosphate buffer at 4 °C for 2 h. Samples were then dehydrated in
1126 ethanol and critically point-dried using a Leica EM CPD300 (Leica, Germany). Samples were
1127 then mounted and sputter coated with platinum (15 nm) using a Cressington 108 sputter coater
1128 (Cressington, United Kingdom). The images were taken with a Quanta250 field-emission
1129 scanning electron microscope (FEI, The Netherlands).
1130
1131 **Endogenous cAMP measurement**
1132 To measure the cAMP levels in mouse cochlea or utricle or in HEK293 cells, the isolated
1133 cochlear or utricle explants or HEK293 cells transfected with Flag-LPHN2 were treated without
1134 or with LPHN2-M-beads for 15 min in the presence of IBMX. The harvested cochlear or utricle
1135 explants or HEK293 cells were homogenized in cold 0.1 M HCl and centrifuged at 12000 rpm
1136 for 10 min to remove the particulates. The supernatants were collected and neutralized with 1M
1137 NaOH. The cAMP levels were determined using cAMP ELISA Kit (R&D systems, KGE012B)
1138 according to manufacturer's instructions.
1139

1140 **Structural modelling of LPHN2 and virtual screening for LPHN2 inhibitors**

1141 Homology modelling of LPHN2 was performed with the online program SWISS-MODEL
1142 (https://swissmodel.expasy.org/)(Waterhouse et al., 2018). First, the primary amino acid
1143 sequence of human LPHN2 (E835-C1098) was uploaded to the program, then the inactive
1144 CD97 structure was also uploaded as template for homology modelling of LPHN2 structure
1145 (Mao et al., 2024b). Model was built based on the target-template alignment using ProMod3.
1146 Coordinates which are conserved between the target and the template are copied from the
1147 template to the model. Insertions and deletions are remodeled using a fragment library. Side
1148 chains are then rebuilt. Finally, the geometry of the resulting model is regularized by using a
1149 force field. The global and per-residue model quality has been assessed using the QMEAN
1150 scoring function (Studer et al., 2020). The interactions between LPHN2 (I840-G1135) and
1151 TMC1 (C161-Q760) was simulated using the online program ColabFold v1.5.5 (AlphaFold2
1152 using MMseqs2) (Mirdita et al., 2022).

1153 The predicted ligand binding pocket in modelled structure of LPHN2 was analyzed through
1154 *SiteMap* algorithm with Maestro (version 13.4, Schrödinger LLC, New York, NY) software
1155 (Halgren, 2009). All atoms in modelled LPHN2 structures were considered as the receptor. The
1156 grid spacing was set to 0.7 Å, and points that border on too many assigned philic points were
1157 excluded. Each pocket required at least 15 site points, and top four potential binding pockets
1158 were identified and analyzed. Maestro software was employed to perform virtual screening.
1159 The modelled structure of LPHN2 was used to construct the virtual screening model. First, the
1160 Protein Preparation Workflow was used to prepare the modelled LPHN2 structure with default
1161 settings. Then, the docking grid of the predicted top 1 binding pocket was generated by the
1162 Receptor Grid Generation panel with default settings. Subsequently, the 1000,000 molecules in
1163 our designed compound database were prepared using the LigPrep panel (LigPrep, version 2.3)
1164 in Maestro with the following settings: the ionized states and tautomers were generated by Epik
1165 algorithm at pH 7.0 ± 2.0; The chiralities were retained for ligands with specified chiralities;
1166 The maximum number of stereoisomers for each ligand was set to 32. The OPLS4 force field
1167 was used for energy minimization. Finally, molecular docking was performed using the Ligand
1168 Docking panel with XP (extra precision) mode. In this process, all the parameters were set as
1169 the default settings. Clustering analysis was performed using “clustering Molecules” protocols

integrated in Pipeline Pilot, version 7.5 (Pipeline Pilot; Accelrys SoftwareInc., San Diego, CA).

BRET assay

G protein dissociation BRET assay

To investigate the force-induced G protein activation of LPHN2, the G protein dissociation BRET assay was performed as previously described (Yang et al., 2021; Yang et al., 2024). Briefly, HEK293 cells co-transfected with either LPHN2 or its mutations, along with Gs or Gi BRET probes were incubated for 24 hours. The cells were then plated into a 96-well microplate at a density of 5×10^5 cells per well. The cells were incubated for another 24 hours at 37°C before being subjected to mechanical stimulation with a force of 3pN for 3 minutes. Following the mechanical stimulation, coelenterazine 400a (Interchim Cayman) at a final concentration of 5 μM was added, and BRET signals were measured using a Mithras LB940 multimode reader (Berthold Technologies). The BRET signal was determined as the ratio of light emission at 510 nm to that at 400 nm.

LPHN2-TMC1 BRET assay

To detect the constitutive interaction between LPHN2 and TMC1, HEK293 cells were transfected with a fixed amount of Myc-VLGR1a and LPHN2-Nluc (LPHN2-ICL1-Nluc, LPHN2-ICL2-Nluc, LPHN2-ICL3-Nluc or LPHN2-Cter-Nluc) along with an increasing concentration of TMC1-YFP (N ter-YFP-TMC1 or TMC1-Cter-YFP) and incubated for 48 h at 37 °C. Then the cells were digested, centrifuged and resuspended in BRET buffer (140 mM NaCl, 2.7 mM KCl, 1 mM $CaCl_2$, 0.9 mM $MgCl_2$, 0.37 mM NaH_2PO_4, 12 mM $NaHCO_3$, 25 mM HEPES and 5.5 mM d-glucose), and then distributed into black-wall clear-bottom 96-well plates at a density of 5×10^4 cells per well. After adding coelenterazine H (a final concentration of 5 mM), the light emissions at 540 nm and 460 nm were recorded using a Mithras LB 940 Multimode Microplate Reader. The BRET signal was calculated as the ratio of the Em540 over Em460. The net BRET was calculated by subtracting the BRET signal obtained in the cells transfected without TMC1-YFP.

For the force-induced interaction between LPHN2 and TMC1, the HEK293 cells transfected with Flag-LPHN2-Nluc, TMC1-YFP and VLGR1a were incubated with buffer containing polylysine-coated Ctrl-beads or Flag-M-beads for 15 min. The cells were stimulated with or

without force for 2 min, and then coelenterazine H (a final concentration of 5 μM) was added, followed by the recording of light emissions at 540 nm and 460 nm as described above. The △BRET was calculated as the BRET signal change due to the force stimulation.

FlAsH-BRET assay

To investigate the force-induced conformational changes in TMC1, HEK293 cells were transfected with Myc-VLGR1a, Flag-LPHN2 and Nluc-TMC1-FlAsH probes (N-Nluc-TMC1-ICL1-FlAsH, N-Nluc-TMC1-ICL2-FlAsH, N-Nluc-TMC1-ICL3-FlAsH, or N-Nluc-TMC1-ICL4-FlAsH) and incubated for 24 h at 37 °C. Then the cells were distributed into 96-well plates at a density of 5×10^4 cells per well. After 24 h, the cells were labeled with FlAsH-EDT2 (a final concentration of 2.5 μM) for 40 min at 37 °C. After washing twice with PBS, the cells were treated with polylysine-coated Ctrl-beads or Flag-M-beads for 15 min in the absence or presence of NF449 (10 μM) or D11 (50 nM). The cells were then stimulated with magnetic force for 2 min. After adding coelenterazine H (a final concentration of 5 μM), the light emissions at 540 nm and 460 nm were recorded. The BRET signal was calculated as the ratio of the Em540 over Em460.

Cell surface ELISA assay

The cell surface expression levels of LPHN2 and its mutants, or TMC1 conformational sensors were determined by cell surface ELISA assay. Briefly, HEK293 cells transiently transfected with N-terminal Flag-tagged wild-type LPHN2 or mutants, or TMC1 conformational sensors in 24-well plates for 48 h were fixed with 4% (w/v) paraformaldehyde and incubated with anti-Flag M2 primary antibody and a secondary goat anti-mouse antibody conjugated to horseradish peroxide. A color reaction was initiated by adding TMB (3,3′,5,5′-Tetramethylbenzidine) solution and stopped by adding an equal volume of 0.25 M HCl. The absorbance at 450 nm of each well was measured to determine the relative expression levels. The transfecting amounts of the plasmids encoding corresponding mutants or conformational sensors were adjusted to enable equal cell-surface expression levels of the target proteins.

Adeno-associated virus preparation and injection

The AAV-ie-*Lphn2pr*-mCherry (3.5×10^{13} genomic copies per ml) and AAV-ie-LPHN2 (3.0

1230 × 10^{13} genomic copies per ml)) were generated by OBiO Technology (Shanghai, China). Both
1231 viruses were modified from the original AAV-ie vectors (Tan et al., 2019). Briefly, for the
1232 construction of AAV-ie-*Lphn2pr*-mCherry, the original CAG promoter in the AAV-ie was
1233 replaced with the promoter region (800 bp) of *Lphn2*, which directs the expression of mCherry
1234 and could be used for the labelling of LPHN2-expressing cochlear hair cells. For in vivo rescue
1235 experiment, the LPHN2-GAIN sequence with an N-terminal 3×Flag tag was inserted into the
1236 AAV-ie-*Lphn2pr*-mCherry vector. An IRES element was placed between the Flag-LPHN2-
1237 GAIN and the mCherry coding sequence. All viral vectors were aliquoted and stored at -80 °C
1238 until use.

1239 For virus injection, *Pou4f3-CreER*$^{+/-}$*Lphn2*$^{+/+}$ or *Pou4f3-CreER*$^{+/-}$*Lphn2*$^{fl/fl}$ mice at P3 were
1240 placed in an ice bath until loss of consciousness and then moved to an ice pad for surgical
1241 procedures. Injections were performed through the round window membrane of left ear of
1242 mouse with a glass micropipette (25 μm) at a speed of 1 μL virus / min controlled by a
1243 micromanipulator UMP3 UltraMicroPump (World Precision Instruments). A total volume of
1244 0.8 μL of the AAV-ie-*Lphn2pr*-mCherry or AAV-ie-LPHN2 virus was injected and then the
1245 incision was closed using veterinary tissue adhesive (Millpledge Ltd, UK). The mice were
1246 placed on a 37 °C warming pad until fully awake.

1247

1248 **Single-cell Ca^{2+} imaging**

1249 The cochlear explants derived from *Pou4f3-CreER*$^{+/-}$*Lphn2*$^{+/+}$ or *Pou4f3-CreER*$^{+/-}$*Lphn2*$^{fl/fl}$
1250 mice were attached to 12-mm round glass coverslips, which were pre-coated with polylysine
1251 and placed in 35-mm dishes. Cochlear explants were incubated with imaging buffer (10 mM
1252 glucose,150 mM NaCl, 5 mM KCl, 1.3 mM $MgCl_2$, 1.2 mM NaH_2PO_4, 3 mM $CaCl_2$, 20 mM
1253 HEPES, pH 7.4) containing 2.5 μM Fura-2 and 0.05 % Pluronic F-127 (Life Technologies) for
1254 15 min at 37 °C. After washing with imaging buffer, the cochlear explants were incubated with
1255 fresh imaging buffer containing LPHN2-M-beads or Ctrl-beads for 20 min at 37 °C to enable
1256 the association of the antibody-coated beads with the target proteins. Then, the dish containing
1257 the cochlear explants was mounted into an Olympus IX71 microscope equipped with a FluoCa
1258 BioHD CMOS camera and a pE-340fura illumination system (coolLED). The cochlear hair
1259 cells labelled by AAV-ie-*Lphn2pr*-mCherry were selected for Ca^{2+} imaging. The F340/F380

1260 ratio of selected cells were recorded while the magnetic force was applied on the LPHN2-M-
1261 beads or Ctrl-beads. Data are recorded and analyzed using the VisiFLUOR Fluorescence Ratio
1262 Imaging System (Visitron Systems).
1263

1264 **Glutamate secretion detection**

1265 To characterize the glutamate secretion from cochlear hair cells, AAV-ie-*hSyn*-R^{ncp}-
1266 iGluSnFR (4×10^{13} genomic copies per ml) were delivered to *Pou4f3-CreER*$^{+/-}$*Lphn2*$^{+/+}$ or
1267 *Pou4f3-CreER*$^{+/-}$*Lphn2*$^{fl/fl}$ mice at P3. A total volume of 0.8 μL of the AAV-ie-*hSyn*-R^{ncp}-
1268 iGluSnFR virus was injected and then the incision was closed using veterinary tissue adhesive
1269 (Millpledge Ltd, UK). The cochlea was isolated at P10 and the explants were incubated with
1270 fresh imaging buffer containing LPHN2-M-beads or Ctrl-beads for 20 min at 37 °C to enable
1271 the association of the antibody-coated beads with the target proteins. Widefield imaging was
1272 performed on an inverted Olympus IX71 microscope equipped with a 200 W metal halide lamp
1273 (PRIOR Lumen), 60× objectives, and a 16-bit QuantEM 512SC electron-multiplying CCD
1274 camera (Photometrics). A filter set of 620/60 nm (emission) and 570 nm (dichroic) was used
1275 for recording cells labelled by AAV-ie-*hSyn*-R^{ncp}-iGluSnFR. The selected cells were recorded
1276 while the magnetic force was applied on the LPHN2-M-beads or Ctrl-beads. Data are recorded
1277 and analyzed using the VisiFLUOR Fluorescence Ratio Imaging System (Visitron Systems).
1278

1279 **Electrophysiology**

1280 AAV-ie-*Lphn2pr*-mCherry was delivered into *Pou4f3-CreER*$^{+/-}$*Lphn2*$^{+/+}$ or *Pou4f3-CreER*$^{+/-}$
1281 *Lphn2*$^{fl/fl}$ mice at P3. The organs of Corti were isolated at P10 and the mCherry-labelled OHCs
1282 and IHCs were selected for electrophysiological studies. Excised cochlear turns were placed in
1283 a recording chamber mounted on an upright microscope (Olympus), and visualized using a 63
1284 x 0.9 NA water-immersion objective and infrared differential interference contrast. MET
1285 currents were recorded using fluid jet assay as described previously (Liu et al., 2019). Briefly,
1286 currents were evoked using a fluid jet from a pipette (tip diameter of 5–10 μm) positioned facing
1287 the staircase side of the hair bundle at a distance of around 5 μm at room temperature. The fluid
1288 jet was driven by a 40-Hz sinusoidal voltage to deflect the hair bundles. The fluid flow was
1289 controlled by a 27-mm-diameter piezoelectric disk driven by a homemade 20 × amplifier that

1290 precisely outputs analog driving voltage. The command signal was generated by an amplifier
1291 (EPC10, HEKA) controlled by the PatchMaster software with a holding potential of –80mV.
1292 Patch pipettes were pulled from borosilicate glass (ITEM #:BF150-86-10, Sutter Instrument
1293 Co.) using a micropipette puller (P-97, Sutter Instrument Co.) to a resistance of 3-5 MΩ. The
1294 pipette solution contained 142 mM KCl, 3.5 mM $MgCl_2$, 1 mM EGTA, 2.5 mM MgATP, 0.1
1295 mM $CaCl_2$, 5 mM HEPES, adjusted to a pH of 7.4 with KOH. The external solution contained
1296 145 mM NaCl, 5.8 mM KCl, 0.9 mM $MgCl_2$, 1.3 mM $CaCl_2$, 0.7 mM NaH_2PO_4, 10 mM HEPES
1297 and 5.6 mM D-glucose, adjusted to a pH of 7.4 with NaOH.
1298 For the electrophysiology in the heterologous system, HEK293 cells transfected with GPCR-
1299 HC1, TMC1 and LPHN2 were plated onto coverslips coated with polylysine. The single
1300 channel currents in HEK293 cells were recorded 24-48 h after transfection. Cell-attached patch
1301 recordings were performed in extracellular solution (140 mM NaCl, 5 mM KCl, 2.5 mM $CaCl_2$,
1302 1 mM $MgCl_2$, 10 mM glucose, 10 mM HEPES, pH 7.4 with NaOH) using 6-8 MΩ resistance
1303 electrodes filled with intracellular solution (140 mM CsCl, 5 mM EGTA and 10 mM HEPES,
1304 pH 7.4 with KOH). The current-voltage (I-V) curves of the spontaneous currents were plotted
1305 and fitted to the response amplitude measured from -80 to +80 mV in 20-mV increments. The
1306 single-channel conductance was obtained through linear fitting of the current-voltage plots. The
1307 inhibitors were added to the bath solution and the channel opening was recorded again from the
1308 same patch. The following inhibitors were tested: ruthenium red (RR, 40 μM), FM1-43 (3 μM),
1309 dihydrostreptomycin (DHS, 0.2 mM), amiloride (0.2 mM), NF449 (20 μM) and D11 (50 nM).
1310 For the force-induced single-channel currents, the cells were incubated with fresh extracellular
1311 solution containing LPHN2-M-beads or CDH23-M-beads for 20 min at 37 °C to enable the
1312 association of the antibody-coated beads with the target proteins. Then, the cell-attached patch
1313 recordings were performed while the magnetic force was applied on the LPHN2-M-beads or
1314 Ctrl-beads.
1315
1316 **Co-immunoprecipitation**
1317 The cochlea from WT mice were ground and lysed with NP40 lysis buffer containing
1318 phosphatase and protease inhibitors. The lysates were immunoprecipitated using LPHN2- or
1319 control-antibody-conjugated agarose overnight at 4 °C. After washing with PBS, the

1320 immunoprecipitated proteins were subjected to electrophoresis and western blotting analysis
1321 using specific antibodies against specific MET channel components, including TMC1,
1322 PCDH15, LHFPL5, and TMIE.
1323

1324 **Mass spectrometry analysis**

1325 The cochlear epithelium derived from wild-type mice were homogenized using NP40 lysis
1326 buffer, supplemented with phosphatase and protease inhibitors. The resulting lysates were
1327 subjected to immunoprecipitation for 4 hours at 4°C using LPHN2-GAIN-bait (LPHN2-GAIN
1328 conjugated to the anti-Flag M2 beads) or control bait (empty anti-Flag M2 beads). After a 30
1329 min treatment with 10% DSP on a shaker, the cross-linking reaction was terminated by the
1330 addition of 1 M Tris (pH 7.5). Following centrifugation at 1000 rpm for 5 min at 4°C, the
1331 precipitated beads were collected and subjected to three washes with a wash buffer (20 mM
1332 HEPES pH 7.5, 4 mM $MgCl_2$, 15% Glycerin, 3 mM $CaCl_2$, 100 mM NaCl, 0.01% MNG, 0.006%
1333 CHS) containing phosphatase and protease inhibitors. The precipitated beads were then eluted
1334 using the wash buffer containing 10 mM EGTA and 0.1 mg/ml Flag peptide, and subsequently
1335 concentrated using a concentrating column. Finally, the samples were stained using a silver
1336 staining kit and digested with trypsin for subsequent mass spectrometry analysis (Shanghai
1337 Applied Protein Technology Co., Ltd).
1338

1339 **Statistical analysis**

1340 All data in the present study were presented as mean ± SEM values with the numbers of mice
1341 or individual experiments indicted in the Figure or Figure legends. Unpaired two-tailed
1342 Student's *t* test was used for the comparison between two groups. Differences between multiple
1343 groups with one or two variables were determined using one-way or two-way ANOVA followed
1344 by Dunnett's post hoc test, respectively. Statistical analysis was performed using GraphPad
1345 Prism 9 software. Significance was defined as $*P < 0.05$, $**P < 0.01$, $***P < 0.001$. No methods
1346 were used to determine whether the data met assumptions of the statistical approach. No power
1347 analysis was performed to determine the sample size. The sample size of mice in each
1348 experiment was determined based on experience from previous studies in our lab.
1349

1350 **References**

1351 Anderson, G.R., Maxeiner, S., Sando, R., Tsetsenis, T., Malenka, R.C., and Sudhof, T.C. (2017).
1352 Postsynaptic adhesion GPCR latrophilin-2 mediates target recognition in entorhinal-hippocampal
1353 synapse assembly. J Cell Biol *216*, 3831-3846.
1354 Angers, S., Salahpour, A., Joly, E., Hilairet, S., Chelsky, D., Dennis, M., and Bouvier, M. (2000).
1355 Detection of beta 2-adrenergic receptor dimerization in living cells using bioluminescence
1356 resonance energy transfer (BRET). Proc Natl Acad Sci U S A *97*, 3684-3689.
1357 Arshavsky, V., and Bownds, M.D. (1992). Regulation of deactivation of photoreceptor G protein by
1358 its target enzyme and cGMP. Nature *357*, 416-417.
1359 Avenarius, M.R., Krey, J.F., Dumont, R.A., Morgan, C.P., Benson, C.B., Vijayakumar, S., Cunningham,
1360 C.L., Scheffer, D.I., Corey, D.P., Muller, U.*, et al.* (2017). Heterodimeric capping protein is required
1361 for stereocilia length and width regulation. J Cell Biol *216*, 3861-3881.
1362 Beurg, M., Cui, R., Goldring, A.C., Ebrahim, S., Fettiplace, R., and Kachar, B. (2018). Variable number
1363 of TMC1-dependent mechanotransducer channels underlie tonotopic conductance gradients in
1364 the cochlea. Nat Commun *9*, 2185.
1365 Beurg, M., Fettiplace, R., Nam, J.H., and Ricci, A.J. (2009). Localization of inner hair cell
1366 mechanotransducer channels using high-speed calcium imaging. Nat Neurosci *12*, 553-558.
1367 Beurg, M., Xiong, W., Zhao, B., Muller, U., and Fettiplace, R. (2015). Subunit determination of the
1368 conductance of hair-cell mechanotransducer channels. Proc Natl Acad Sci U S A *112*, 1589-1594.
1369 Buck, L., and Axel, R. (1991). A novel multigene family may encode odorant receptors: a molecular
1370 basis for odor recognition. Cell *65*, 175-187.
1371 Caprara, G.A., and Peng, A.W. (2022). Mechanotransduction in mammalian sensory hair cells. Mol
1372 Cell Neurosci *120*, 103706.
1373 Chai, R., Kuo, B., Wang, T., Liaw, E.J., Xia, A., Jan, T.A., Liu, Z., Taketo, M.M., Oghalai, J.S., Nusse, R.,
1374 *et al.* (2012). Wnt signaling induces proliferation of sensory precursors in the postnatal mouse
1375 cochlea. Proc Natl Acad Sci U S A *109*, 8167-8172.
1376 Chandrashekar, J., Hoon, M.A., Ryba, N.J., and Zuker, C.S. (2006). The receptors and cells for
1377 mammalian taste. Nature *444*, 288-294.
1378 Chen, T.Y., and Yau, K.W. (1994). Direct modulation by Ca(2+)-calmodulin of cyclic nucleotide-
1379 activated channel of rat olfactory receptor neurons. Nature *368*, 545-548.
1380 Corey, D.P., and Hudspeth, A.J. (1979). Response latency of vertebrate hair cells. Biophys J *26*, 499-
1381 506.
1382 Coupe, C., Oh, Y.M., Dediu, D., and Pellegrino, F. (2019). Different languages, similar encoding
1383 efficiency: Comparable information rates across the human communicative niche. Sci Adv *5*,
1384 eaaw2594.
1385 Cunningham, C.L., Qiu, X., Wu, Z., Zhao, B., Peng, G., Kim, Y.H., Lauer, A., and Muller, U. (2020).
1386 TMIE Defines Pore and Gating Properties of the Mechanotransduction Channel of Mammalian
1387 Cochlear Hair Cells. Neuron *107*, 126-143 e128.
1388 Davare, M.A., Avdonin, V., Hall, D.D., Peden, E.M., Burette, A., Weinberg, R.J., Horne, M.C., Hoshi,
1389 T., and Hell, J.W. (2001). A beta2 adrenergic receptor signaling complex assembled with the Ca2+
1390 channel Cav1.2. Science *293*, 98-101.
1391 Duncan, J.S., Stoller, M.L., Francl, A.F., Tissir, F., Devenport, D., and Deans, M.R. (2017). Celsr1
1392 coordinates the planar polarity of vestibular hair cells during inner ear development. Dev Biol *423*,
1393 126-137.

Fettiplace, R., Furness, D.N., and Beurg, M. (2022). The conductance and organization of the TMC1-containing mechanotransducer channel complex in auditory hair cells. Proc Natl Acad Sci U S A *119*, e2210849119.

Filipek, S., Stenkamp, R.E., Teller, D.C., and Palczewski, K. (2003). G protein-coupled receptor rhodopsin: a prospectus. Annu Rev Physiol *65*, 851-879.

Frank, T., Khimich, D., Neef, A., and Moser, T. (2009). Mechanisms contributing to synaptic Ca2+ signals and their heterogeneity in hair cells. Proc Natl Acad Sci U S A *106*, 4483-4488.

Fu, Y., Huang, Y., Yang, Z., Chen, Y., Zheng, J., Mao, C., Li, Z., Liu, Z., Yu, B., Li, T.*, et al.* (2021). Cartilage oligomeric matrix protein is an endogenous beta-arrestin-2-selective allosteric modulator of AT1 receptor counteracting vascular injury. Cell Res *31*, 773-790.

Giese, A.P.J., Tang, Y.Q., Sinha, G.P., Bowl, M.R., Goldring, A.C., Parker, A., Freeman, M.J., Brown, S.D.M., Riazuddin, S., Fettiplace, R.*, et al.* (2017). CIB2 interacts with TMC1 and TMC2 and is essential for mechanotransduction in auditory hair cells. Nature communications *8*, 43.

Gillespie, P.G., and Hudspeth, A.J. (1991). High-purity isolation of bullfrog hair bundles and subcellular and topological localization of constituent proteins. J Cell Biol *112*, 625-640.

Gillespie, P.G., and Muller, U. (2009). Mechanotransduction by hair cells: models, molecules, and mechanisms. Cell *139*, 33-44.

Guan, Y., Du, H.B., Yang, Z., Wang, Y.Z., Ren, R., Liu, W.W., Zhang, C., Zhang, J.H., An, W.T., Li, N.N.*, et al.* (2023). Deafness-Associated ADGRV1 Mutation Impairs USH2A Stability through Improper Phosphorylation of WHRN and WDSUB1 Recruitment. Adv Sci (Weinh) *10*, e2205993.

Guo, L., Cheng, J., Lian, S., Liu, Q., Lu, Y., Zheng, Y., Zhu, K., Zhang, M., Kong, Y., Zhang, C.*, et al.* (2023). Structural basis of amine odorant perception by a mammal olfactory receptor. Nature *618*, 193-200.

Halgren, T.A. (2009). Identifying and characterizing binding sites and assessing druggability. J Chem Inf Model *49*, 377-389.

Hall, R.A., Premont, R.T., Chow, C.W., Blitzer, J.T., Pitcher, J.A., Claing, A., Stoffel, R.H., Barak, L.S., Shenolikar, S., Weinman, E.J.*, et al.* (1998). The beta2-adrenergic receptor interacts with the Na+/H+-exchanger regulatory factor to control Na+/H+ exchange. Nature *392*, 626-630.

Harikumar, K.G., Wootten, D., Pinon, D.I., Koole, C., Ball, A.M., Furness, S.G., Graham, B., Dong, M., Christopoulos, A., Miller, L.J.*, et al.* (2012). Glucagon-like peptide-1 receptor dimerization differentially regulates agonist signaling but does not affect small molecule allostery. Proc Natl Acad Sci U S A *109*, 18607-18612.

Hu, Q.X., Dong, J.H., Du, H.B., Zhang, D.L., Ren, H.Z., Ma, M.L., Cai, Y., Zhao, T.C., Yin, X.L., Yu, X.*, et al.* (2014). Constitutive Galphai coupling activity of very large G protein-coupled receptor 1 (VLGR1) and its regulation by PDZD7 protein. J Biol Chem *289*, 24215-24225.

Hudspeth, A.J. (2014). Integrating the active process of hair cells with cochlear function. Nat Rev Neurosci *15*, 600-614.

Hudspeth, A.J., and Corey, D.P. (1977). Sensitivity, polarity, and conductance change in the response of vertebrate hair cells to controlled mechanical stimuli. Proc Natl Acad Sci U S A *74*, 2407-2411.

Hudspeth, A.J., and Jacobs, R. (1979). Stereocilia mediate transduction in vertebrate hair cells (auditory system/cilium/vestibular system). Proc Natl Acad Sci U S A *76*, 1506-1509.

Jaime Tobon, L.M., and Moser, T. (2023). Ca(2+) regulation of glutamate release from inner hair cells of hearing mice. Proc Natl Acad Sci U S A *120*, e2311539120.

1438 Jeong, H., Clark, S., Goehring, A., Dehghani-Ghahnaviyeh, S., Rasouli, A., Tajkhorshid, E., and
1439 Gouaux, E. (2022). Structures of the TMC-1 complex illuminate mechanosensory transduction.
1440 Nature *610*, 796-803.
1441 Jia, Y., Zhao, Y., Kusakizako, T., Wang, Y., Pan, C., Zhang, Y., Nureki, O., Hattori, M., and Yan, Z.
1442 (2020). TMC1 and TMC2 Proteins Are Pore-Forming Subunits of Mechanosensitive Ion Channels.
1443 Neuron *105*, 310-321 e313.
1444 Kaupp, U.B. (2010). Olfactory signalling in vertebrates and insects: differences and commonalities.
1445 Nat Rev Neurosci *11*, 188-200.
1446 Kawashima, Y., Géléoc, G.S., Kurima, K., Labay, V., Lelli, A., Asai, Y., Makishima, T., Wu, D.K., Della
1447 Santina, C.C., Holt, J.R.*, et al.* (2011). Mechanotransduction in mouse inner ear hair cells requires
1448 transmembrane channel-like genes. J Clin Invest *121*, 4796-4809.
1449 Komolov, K.E., Du, Y., Duc, N.M., Betz, R.M., Rodrigues, J., Leib, R.D., Patra, D., Skiniotis, G., Adams,
1450 C.M., Dror, R.O.*, et al.* (2017). Structural and Functional Analysis of a beta(2)-Adrenergic Receptor
1451 Complex with GRK5. Cell *169*, 407-421 e416.
1452 Liang, X., Qiu, X., Dionne, G., Cunningham, C.L., Pucak, M.L., Peng, G., Kim, Y.H., Lauer, A., Shapiro,
1453 L., and Müller, U. (2021). CIB2 and CIB3 are auxiliary subunits of the mechanotransduction channel
1454 of hair cells. Neuron *109*, 2131-2149.e2115.
1455 Lin, H., Xiao, P., Bu, R.Q., Guo, S., Yang, Z., Yuan, D., Zhu, Z.L., Zhang, C.X., He, Q.T., Zhang, C.*, et*
1456 *al.* (2022). Structures of the ADGRG2-G(s) complex in apo and ligand-bound forms. Nat Chem Biol
1457 *18*, 1196-1203.
1458 Liu, C.H., Gong, Z., Liang, Z.L., Liu, Z.X., Yang, F., Sun, Y.J., Ma, M.L., Wang, Y.J., Ji, C.R., Wang, Y.H.*,*
1459 *et al.* (2017). Arrestin-biased AT1R agonism induces acute catecholamine secretion through TRPC3
1460 coupling. Nature communications *8*, 14335.
1461 Liu, S., Wang, S., Zou, L., Li, J., Song, C., Chen, J., Hu, Q., Liu, L., Huang, P., and Xiong, W. (2019).
1462 TMC1 is an essential component of a leak channel that modulates tonotopy and excitability of
1463 auditory hair cells in mice. Elife *8*.
1464 Mao, C., Zhao, R.J., Dong, Y.J., Gao, M., Chen, L.N., Zhang, C., Xiao, P., Guo, J., Qin, J., Shen, D.D.*,*
1465 *et al.* (2024a). Conformational transitions and activation of the adhesion receptor CD97. Mol Cell.
1466 Mao, C., Zhao, R.J., Dong, Y.J., Gao, M., Chen, L.N., Zhang, C., Xiao, P., Guo, J., Qin, J., Shen, D.D.*,*
1467 *et al.* (2024b). Conformational transitions and activation of the adhesion receptor CD97. Mol Cell
1468 *84*, 570-583 e577.
1469 McGee, J., Goodyear, R.J., McMillan, D.R., Stauffer, E.A., Holt, J.R., Locke, K.G., Birch, D.G., Legan,
1470 P.K., White, P.C., Walsh, E.J.*, et al.* (2006). The very large G-protein-coupled receptor VLGR1: a
1471 component of the ankle link complex required for the normal development of auditory hair
1472 bundles. J Neurosci *26*, 6543-6553.
1473 Mecca, A.A., Caprara, G.A., and Peng, A.W. (2022). cAMP and voltage modulate rat auditory
1474 mechanotransduction by decreasing the stiffness of gating springs. Proc Natl Acad Sci U S A *119*,
1475 e2107567119.
1476 Mehta, V., Pang, K.L., Rozbesky, D., Nather, K., Keen, A., Lachowski, D., Kong, Y., Karia, D.,
1477 Ameismeier, M., Huang, J.*, et al.* (2020). The guidance receptor plexin D1 is a mechanosensor in
1478 endothelial cells. Nature *578*, 290-295.
1479 Meyer, A.C., Frank, T., Khimich, D., Hoch, G., Riedel, D., Chapochnikov, N.M., Yarin, Y.M., Harke, B.,
1480 Hell, S.W., Egner, A.*, et al.* (2009). Tuning of synapse number, structure and function in the cochlea.
1481 Nat Neurosci *12*, 444-453.

Mirdita, M., Schutze, K., Moriwaki, Y., Heo, L., Ovchinnikov, S., and Steinegger, M. (2022). ColabFold: making protein folding accessible to all. Nat Methods *19*, 679-682.

Nakamura, T., and Gold, G.H. (1987). A cyclic nucleotide-gated conductance in olfactory receptor cilia. Nature *325*, 442-444.

Pan, B., Akyuz, N., Liu, X.P., Asai, Y., Nist-Lund, C., Kurima, K., Derfler, B.H., Gyorgy, B., Limapichat, W., Walujkar, S.*, et al.* (2018). TMC1 Forms the Pore of Mechanosensory Transduction Channels in Vertebrate Inner Ear Hair Cells. Neuron *99*, 736-753 e736.

Pan, B., Geleoc, G.S., Asai, Y., Horwitz, G.C., Kurima, K., Ishikawa, K., Kawashima, Y., Griffith, A.J., and Holt, J.R. (2013). TMC1 and TMC2 are components of the mechanotransduction channel in hair cells of the mammalian inner ear. Neuron *79*, 504-515.

Peelle, J.E., and Davis, M.H. (2012). Neural Oscillations Carry Speech Rhythm through to Comprehension. Front Psychol *3*, 320.

Petitpre, C., Faure, L., Uhl, P., Fontanet, P., Filova, I., Pavlinkova, G., Adameyko, I., Hadjab, S., and Lallemend, F. (2022). Single-cell RNA-sequencing analysis of the developing mouse inner ear identifies molecular logic of auditory neuron diversification. Nat Commun *13*, 3878.

Qiu, X., and Muller, U. (2022). Sensing sound: Cellular specializations and molecular force sensors. Neuron *110*, 3667-3687.

Ranum, P.T., Goodwin, A.T., Yoshimura, H., Kolbe, D.L., Walls, W.D., Koh, J.Y., He, D.Z.Z., and Smith, R.J.H. (2019). Insights into the Biology of Hearing and Deafness Revealed by Single-Cell RNA Sequencing. Cell Rep *26*, 3160-3171 e3163.

Santos-Cortez, R.L., Lee, K., Giese, A.P., Ansar, M., Amin-Ud-Din, M., Rehn, K., Wang, X., Aziz, A., Chiu, I., Hussain Ali, R.*, et al.* (2014). Adenylate cyclase 1 (ADCY1) mutations cause recessive hearing impairment in humans and defects in hair cell function and hearing in zebrafish. Hum Mol Genet *23*, 3289-3298.

Scholz, N., Dahse, A.K., Kemkemer, M., Bormann, A., Auger, G.M., Vieira Contreras, F., Ernst, L.F., Staake, H., Korner, M.B., Buhlan, M.*, et al.* (2023). Molecular sensing of mechano- and ligand-dependent adhesion GPCR dissociation. Nature *615*, 945-953.

Scholz, N., Gehring, J., Guan, C., Ljaschenko, D., Fischer, R., Lakshmanan, V., Kittel, R.J., and Langenhan, T. (2015). The adhesion GPCR latrophilin/CIRL shapes mechanosensation. Cell Rep *11*, 866-874.

Scholz, N., Guan, C., Nieberler, M., Grotemeyer, A., Maiellaro, I., Gao, S., Beck, S., Pawlak, M., Sauer, M., Asan, E.*, et al.* (2017). Mechano-dependent signaling by Latrophilin/CIRL quenches cAMP in proprioceptive neurons. Elife *6*.

Shi, F., Hu, L., and Edge, A.S. (2013). Generation of hair cells in neonatal mice by beta-catenin overexpression in Lgr5-positive cochlear progenitors. Proc Natl Acad Sci U S A *110*, 13851-13856.

Shi, T., Beaulieu, M.O., Saunders, L.M., Fabian, P., Trapnell, C., Segil, N., Crump, J.G., and Raible, D.W. (2023). Single-cell transcriptomic profiling of the zebrafish inner ear reveals molecularly distinct hair cell and supporting cell subtypes. Elife *12*.

Shukla, A.K., Westfield, G.H., Xiao, K., Reis, R.I., Huang, L.Y., Tripathi-Shukla, P., Qian, J., Li, S., Blanc, A., Oleskie, A.N.*, et al.* (2014). Visualization of arrestin recruitment by a G-protein-coupled receptor. Nature *512*, 218-222.

Smith, S.O. (2023). Mechanism of Activation of the Visual Receptor Rhodopsin. Annu Rev Biophys *52*, 301-317.

Studer, G., Rempfer, C., Waterhouse, A.M., Gumienny, R., Haas, J., and Schwede, T. (2020).

QMEANDisCo-distance constraints applied on model quality estimation. Bioinformatics *36*, 1765-1771.

Sun, S., Babola, T., Pregernig, G., So, K.S., Nguyen, M., Su, S.M., Palermo, A.T., Bergles, D.E., Burns, J.C., and Muller, U. (2018). Hair Cell Mechanotransduction Regulates Spontaneous Activity and Spiral Ganglion Subtype Specification in the Auditory System. Cell *174*, 1247-1263 e1215.

Tan, F., Chu, C., Qi, J., Li, W., You, D., Li, K., Chen, X., Zhao, W., Cheng, C., Liu, X.*, et al.* (2019). AAV-ie enables safe and efficient gene transfer to inner ear cells. Nat Commun *10*, 3733.

Tang, Y.Q., Lee, S.A., Rahman, M., Vanapalli, S.A., Lu, H., and Schafer, W.R. (2020). Ankyrin Is An Intracellular Tether for TMC Mechanotransduction Channels. Neuron *107*, 112-125 e110.

Wang, X., Liu, S., Cheng, Q., Qu, C., Ren, R., Du, H., Li, N., Yan, K., Wang, Y., Xiong, W.*, et al.* (2023). CIB2 and CIB3 Regulate Stereocilia Maintenance and Mechanoelectrical Transduction in Mouse Vestibular Hair Cells. J Neurosci *43*, 3219-3231.

Wang, Y., Guo, N., and Nathans, J. (2006). The role of Frizzled3 and Frizzled6 in neural tube closure and in the planar polarity of inner-ear sensory hair cells. J Neurosci *26*, 2147-2156.

Waterhouse, A., Bertoni, M., Bienert, S., Studer, G., Tauriello, G., Gumienny, R., Heer, F.T., de Beer, T.A.P., Rempfer, C., Bordoli, L.*, et al.* (2018). SWISS-MODEL: homology modelling of protein structures and complexes. Nucleic Acids Res *46*, W296-W303.

Weston, M.D., Luijendijk, M.W., Humphrey, K.D., Moller, C., and Kimberling, W.J. (2004). Mutations in the VLGR1 gene implicate G-protein signaling in the pathogenesis of Usher syndrome type II. Am J Hum Genet *74*, 357-366.

Wu, J., Abdelfattah, A.S., Zhou, H., Ruangkittisakul, A., Qian, Y., Ballanyi, K., and Campbell, R.E. (2018). Genetically Encoded Glutamate Indicators with Altered Color and Topology. ACS Chem Biol *13*, 1832-1837.

Wu, Z., Grillet, N., Zhao, B., Cunningham, C., Harkins-Perry, S., Coste, B., Ranade, S., Zebarjadi, N., Beurg, M., Fettiplace, R.*, et al.* (2017). Mechanosensory hair cells express two molecularly distinct mechanotransduction channels. Nat Neurosci *20*, 24-33.

Xiong, W., Grillet, N., Elledge, H.M., Wagner, T.F., Zhao, B., Johnson, K.R., Kazmierczak, P., and Müller, U. (2012). TMHS is an integral component of the mechanotransduction machinery of cochlear hair cells. Cell *151*, 1283-1295.

Yang, F., Guo, L., Li, Y., Wang, G., Wang, J., Zhang, C., Fang, G.X., Chen, X., Liu, L., Yan, X.*, et al.* (2021). Structure, function and pharmacology of human itch receptor complexes. Nature *600*, 164-169.

Yang, Z., Cheng, J., Shang, P., Sun, J.P., and Yu, X. (2023). Emerging roles of olfactory receptors in glucose metabolism. Trends Cell Biol *33*, 463-476.

Yang, Z., Wang, J.Y., Yang, F., Zhu, K.K., Wang, G.P., Guan, Y., Ning, S.L., Lu, Y., Li, Y., Zhang, C.*, et al.* (2024). Structure of GPR101-Gs enables identification of ligands with rejuvenating potential. Nat Chem Biol *20*, 484-492.

Yang, Z., Zhou, S.H., Zhang, Q.Y., Song, Z.C., Liu, W.W., Sun, Y., Wang, M.W., Zhu, K.K., Guan, Y., Qi, J.Y., et al. (2024). A force-sensitive adhesion GPCR is indispensable in normal equilibrioception （attached as supplemental file to this submission ）.

Yau, K.W., and Hardie, R.C. (2009). Phototransduction motifs and variations. Cell *139*, 246-264.

Zhang, X., Mak, S., Li, L., Parra, A., Denlinger, B., Belmonte, C., and McNaughton, P.A. (2012). Direct inhibition of the cold-activated TRPM8 ion channel by Galphaq. Nat Cell Biol *14*, 851-858.

Zhang, Y., Hoon, M.A., Chandrashekar, J., Mueller, K.L., Cook, B., Wu, D., Zuker, C.S., and Ryba, N.J.

(2003). Coding of sweet, bitter, and umami tastes: different receptor cells sharing similar signaling pathways. Cell *112*, 293-301.

Zhao, B., Wu, Z., Grillet, N., Yan, L., Xiong, W., Harkins-Perry, S., and Müller, U. (2014). TMIE is an essential component of the mechanotransduction machinery of cochlear hair cells. Neuron *84*, 954-967.

Zheng, W., and Holt, J.R. (2021). The Mechanosensory Transduction Machinery in Inner Ear Hair Cells. Annu Rev Biophys *50*, 31-51.

Figure 1

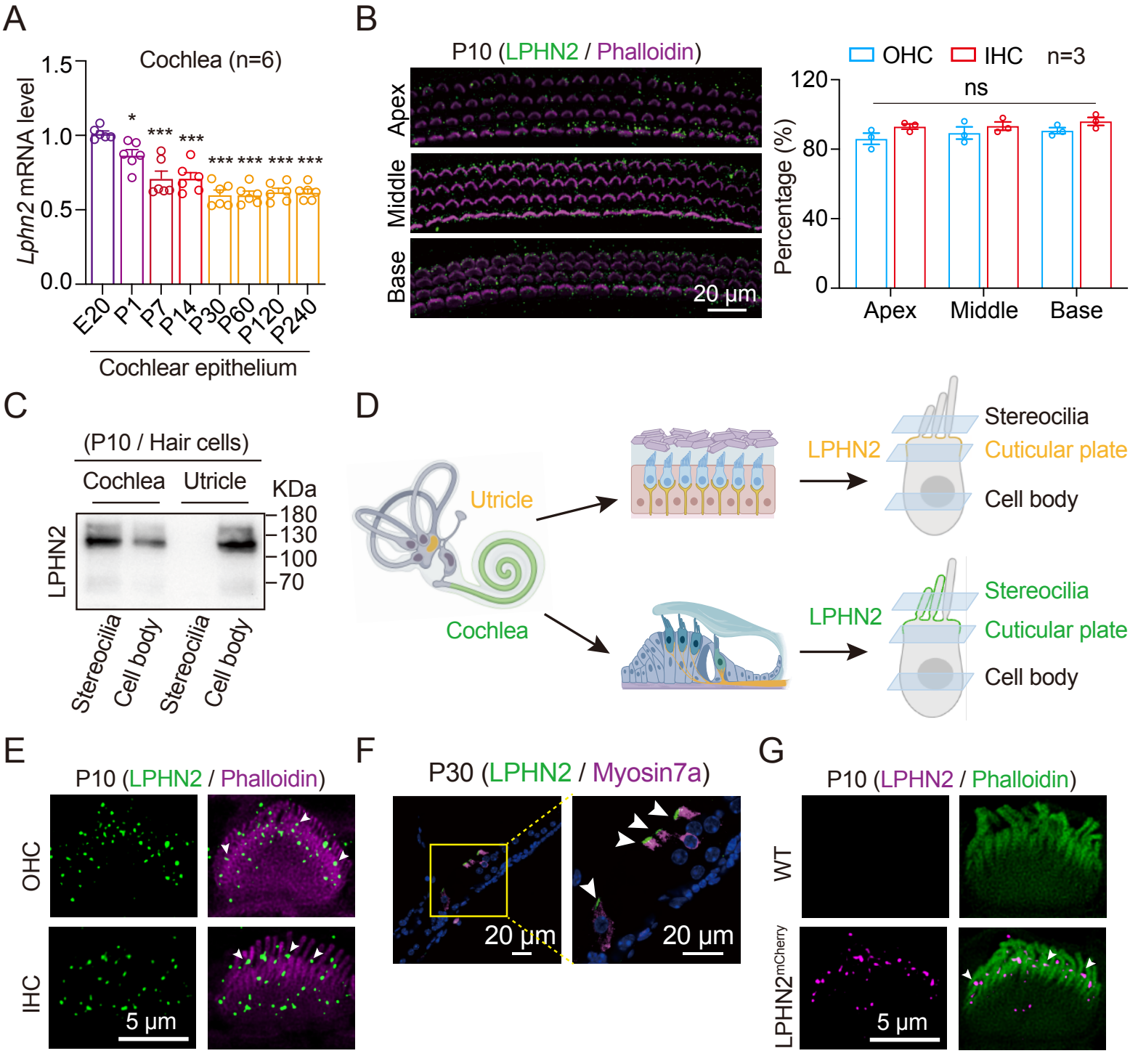
A
Cochlea (n=6)
Lphn2 mRNA level
1.5
1.0
0.5
0.0
*
***
***
***
***
***
***
E20
P1
P7
P14
P30
P60
P120
P240
Cochlear epithelium
B
P10 (LPHN2 / Phalloidin)
Apex
Middle
Base
20 μm
OHC
IHC
n=3
ns
Percentage (%)
120
80
40
0
Apex
Middle
Base
C
(P10 / Hair cells)
Cochlea
Utricle
KDa
180
130
100
70
LPHN2
Stereocilia
Cell body
Stereocilia
Cell body
D
Utricle
Cochlea
LPHN2
Stereocilia
Cuticular plate
Cell body
LPHN2
Stereocilia
Cuticular plate
Cell body
E
P10 (LPHN2 / Phalloidin)
OHC
IHC
5 μm
F
P30 (LPHN2 / Myosin7a)
20 μm
20 μm
G
P10 (LPHN2 / Phalloidin)
WT
LPHN2mCherry
5 μm

Figure 2

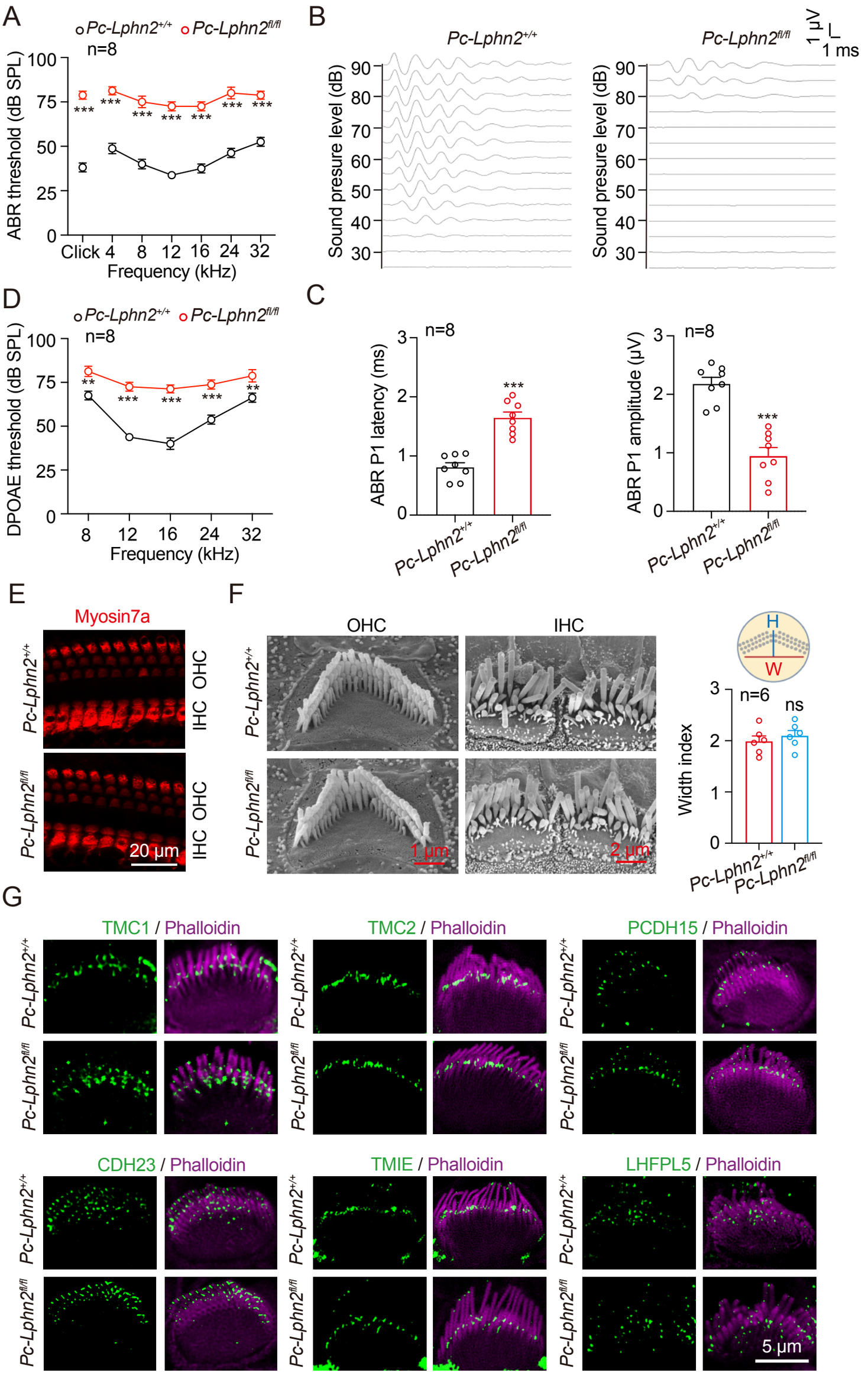
A
Pc-Lphn2+/+
Pc-Lphn2fl/fl
n=8
ABR threshold (dB SPL)
Click 4 8 12 16 24 32
Frequency (kHz)
B
Pc-Lphn2+/+
Pc-Lphn2fl/fl
1 μV
1 ms
Sound presure level (dB)
D
DPOAE threshold (dB SPL)
Frequency (kHz)
C
ABR P1 latency (ms)
ABR P1 amplitude (μV)
E
Myosin7a
OHC
IHC
20 μm
F
OHC
IHC
1 μm
2 μm
H
W
Width index
n=6
ns
G
TMC1 / Phalloidin
TMC2 / Phalloidin
PCDH15 / Phalloidin
CDH23 / Phalloidin
TMIE / Phalloidin
LHFPL5 / Phalloidin
5 μm

Figure 3

A

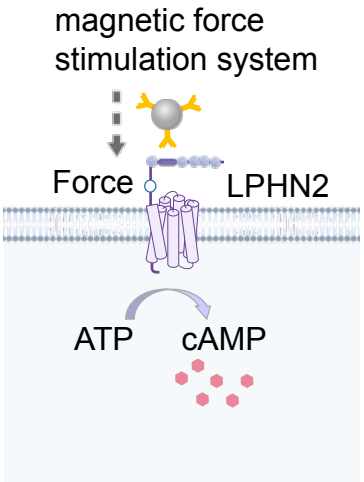

B

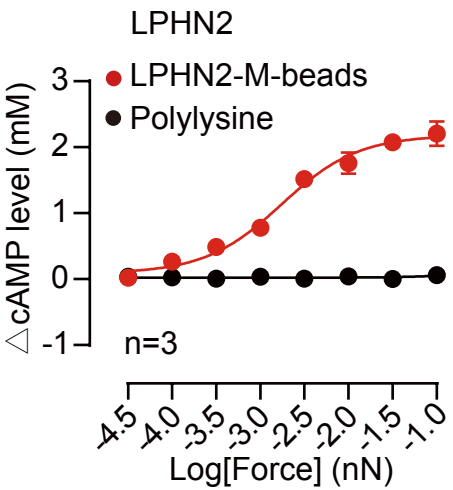

C

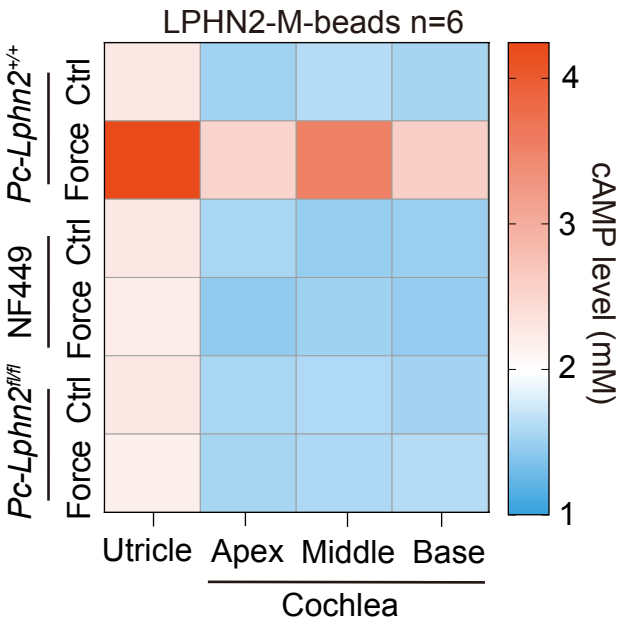

D

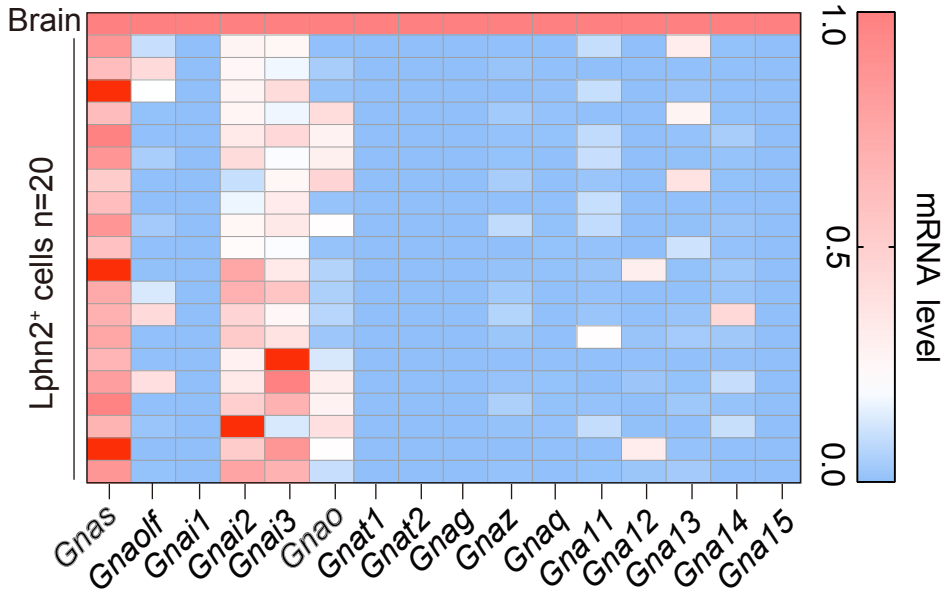

Figure 4

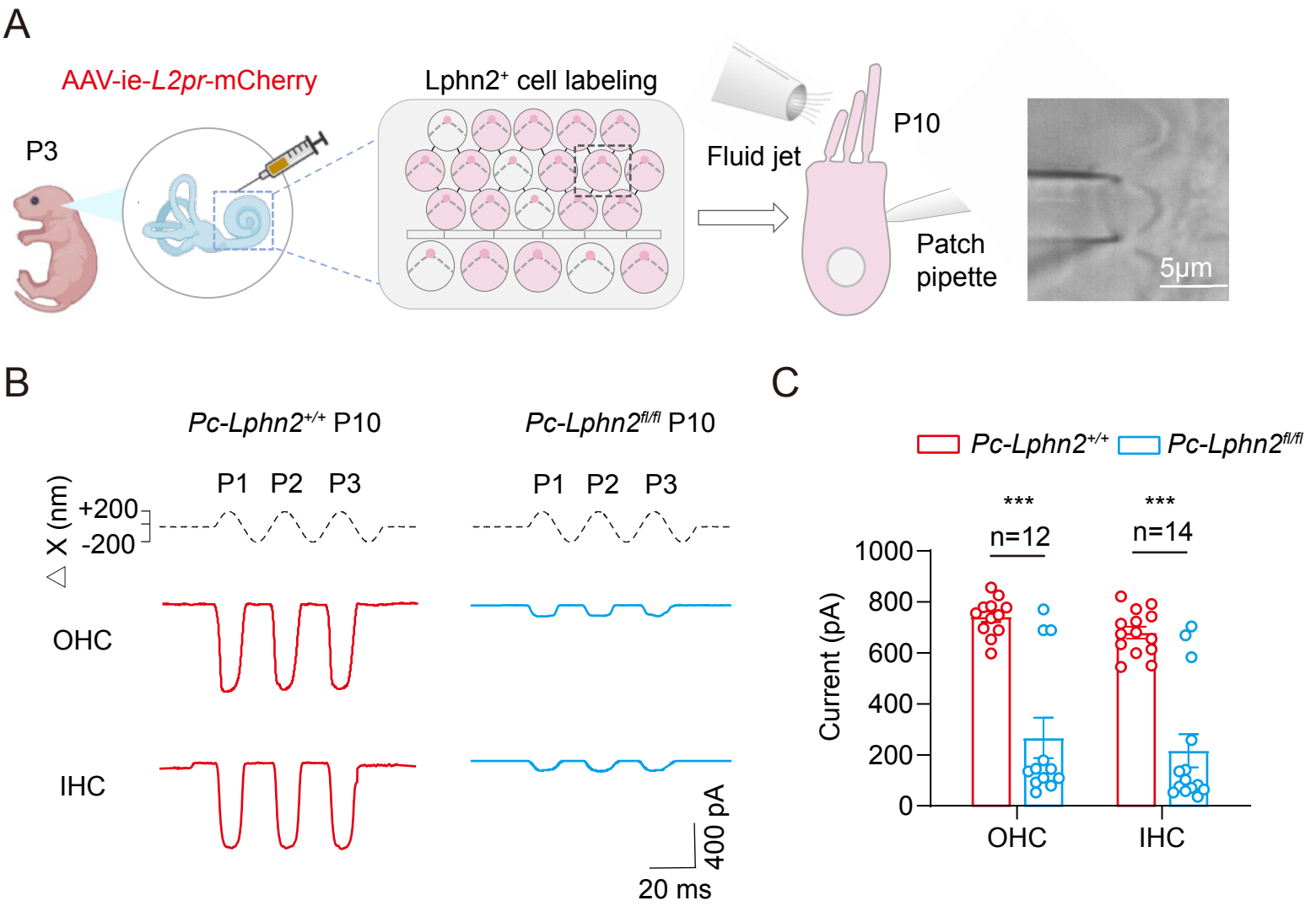
A
AAV-ie-L2pr-mCherry
P3
Lphn2+ cell labeling
Fluid jet
P10
Patch
pipette
5μm
B
Pc-Lphn2+/+ P10
Pc-Lphn2fl/fl P10
P1 P2 P3
P1 P2 P3
△ X (nm)
+200
-200
OHC
IHC
400 pA
20 ms
C
Pc-Lphn2+/+
Pc-Lphn2fl/fl
***
***
n=12
n=14
Current (pA)
1000
800
600
400
200
0
OHC
IHC

Figure 5

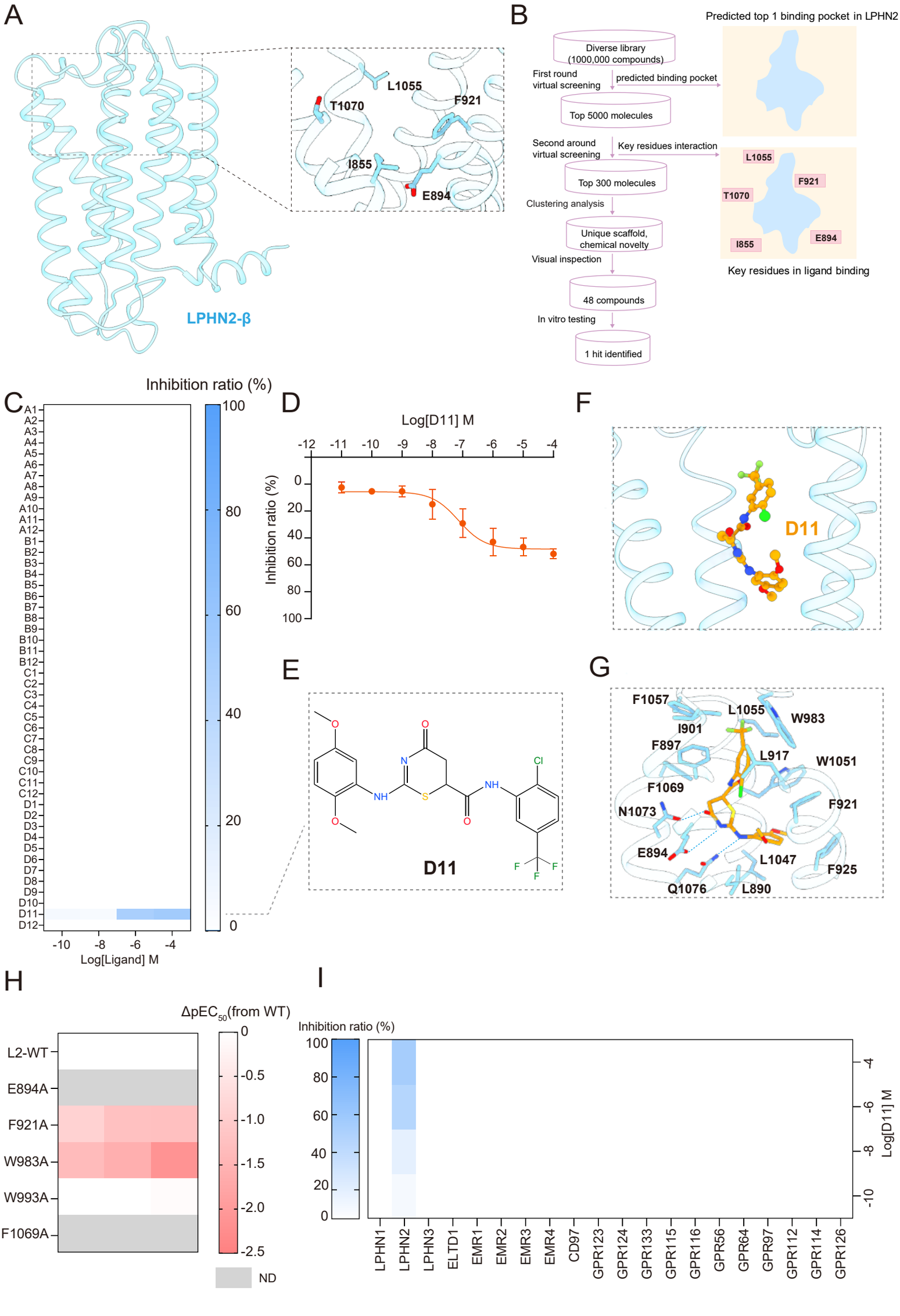
A
T1070
L1055
F921
I855
E894
LPHN2-β
B
Diverse library (1000,000 compounds)
First round virtual screening
predicted binding pocket
Top 5000 molecules
Second around virtual screening
Key residues interaction
Top 300 molecules
Clustering analysis
Unique scaffold, chemical novelty
Visual inspection
48 compounds
In vitro testing
1 hit identified
Predicted top 1 binding pocket in LPHN2
Key residues in ligand binding
C
Inhibition ratio (%)
Log[Ligand] M
D
Log[D11] M
Inhibition ratio (%)
E
D11
F
D11
G
F1057
L1055
W983
I901
F897
L917
W1051
F1069
F921
N1073
E894
L1047
F925
Q1076
L890
H
ΔpEC50(from WT)
L2-WT
E894A
F921A
W983A
W993A
F1069A
ND
I
Inhibition ratio (%)
Log[D11] M
LPHN1
LPHN2
LPHN3
ELTD1
EMR1
EMR2
EMR3
EMR4
CD97
GPR123
GPR124
GPR133
GPR115
GPR116
GPR56
GPR64
GPR97
GPR112
GPR114
GPR126

Figure 6

A

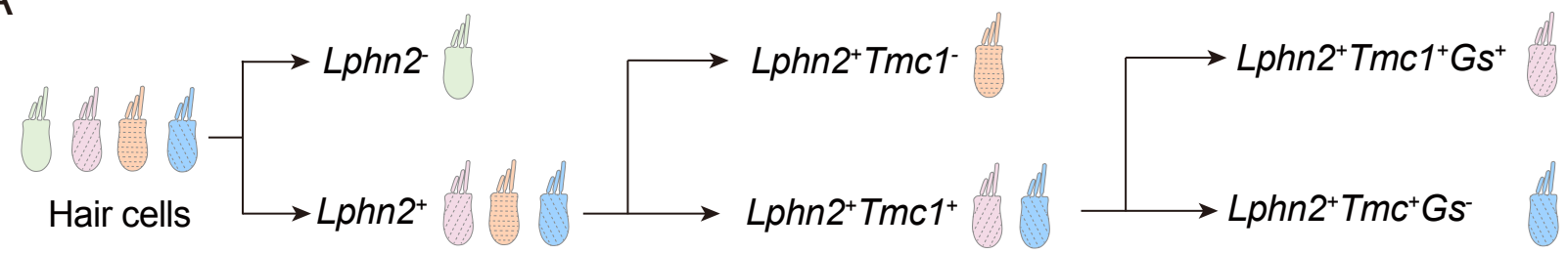

	Lphn2-Tmc1+	Lphn2+Tmc1-	Lphn2+Tmc1+Gs+	Lphn2+Tmc1+Gs-
Percentage	18.7%	5.3%	46.7%	29.3%

B

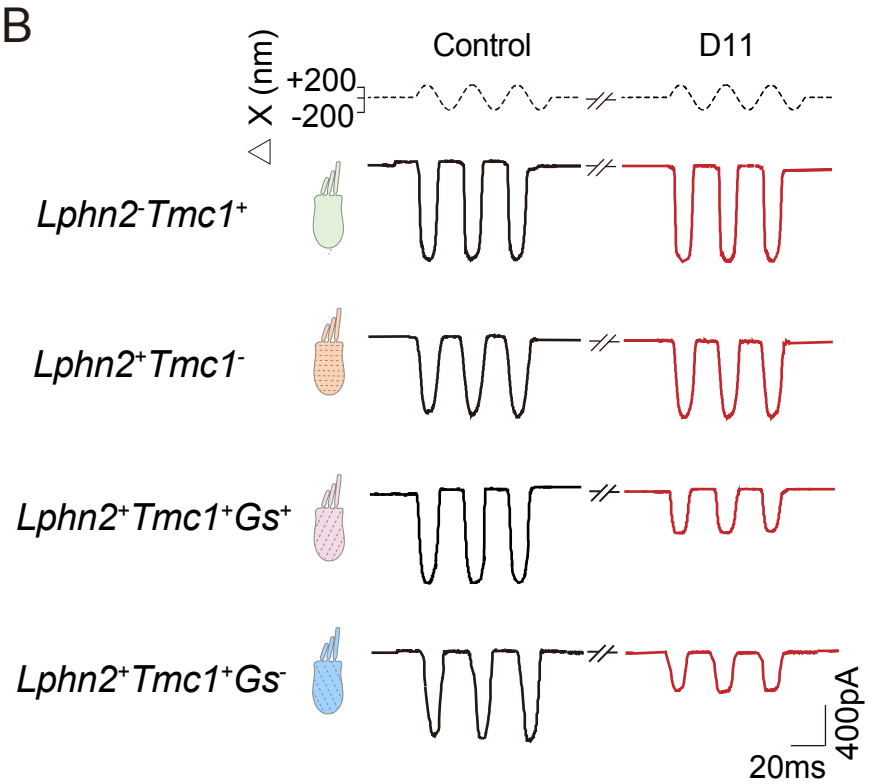

C

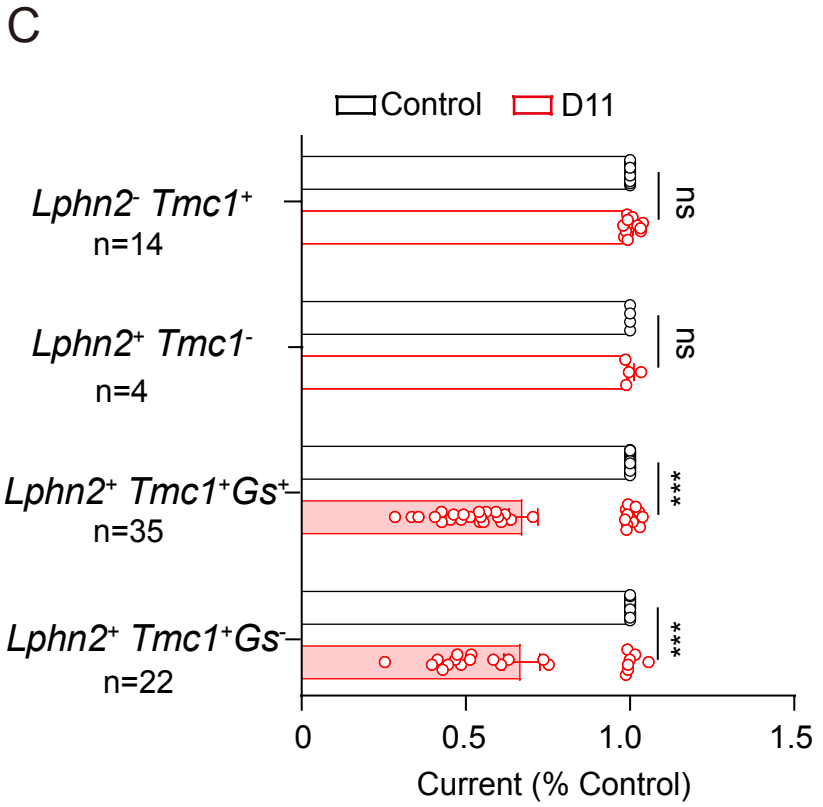

D

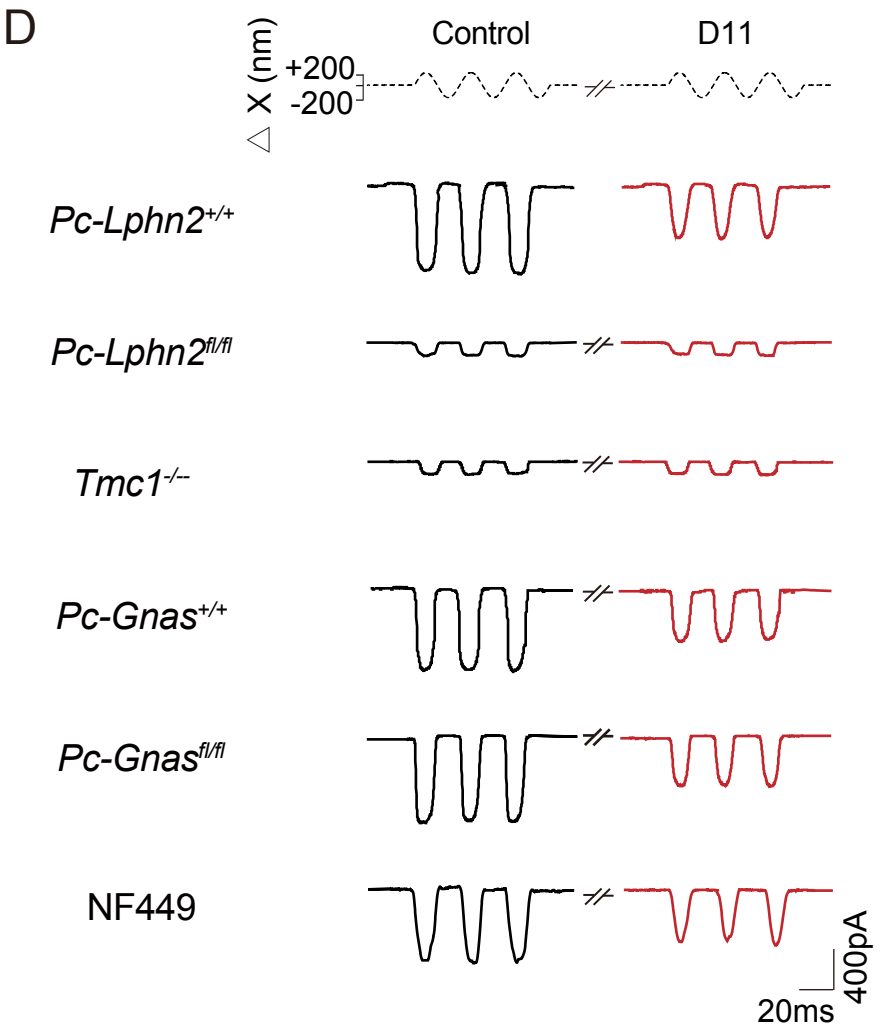

E

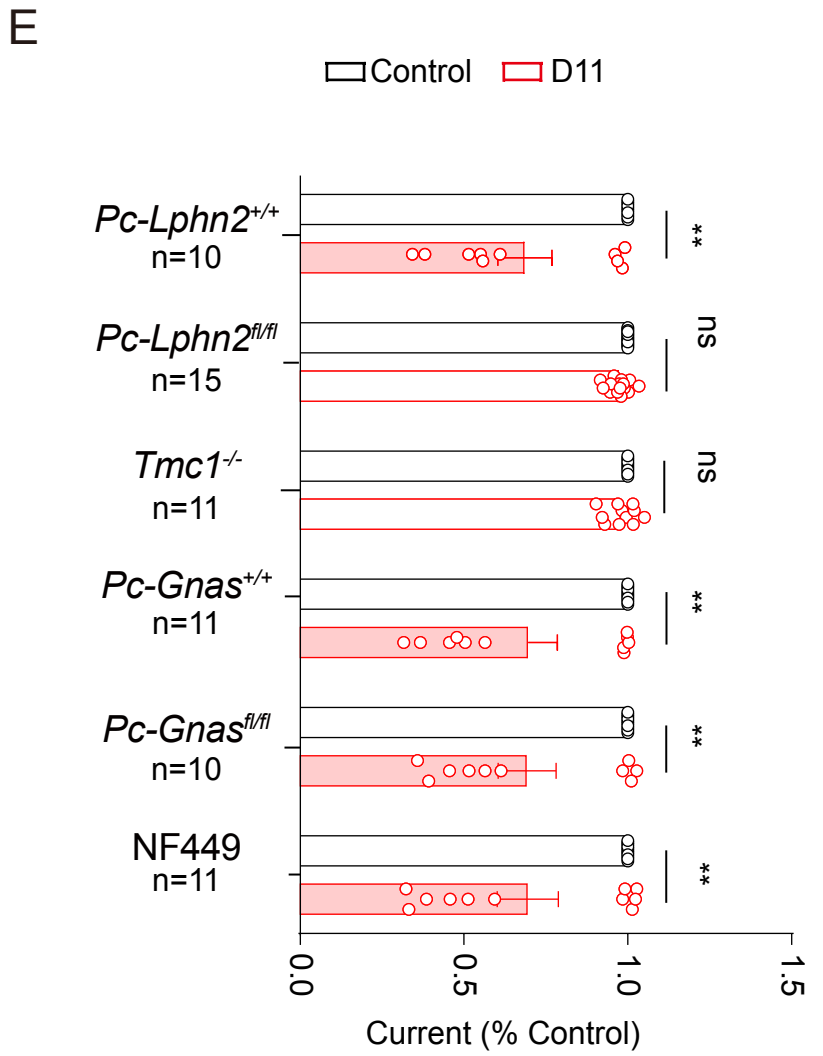

Figure 7

A

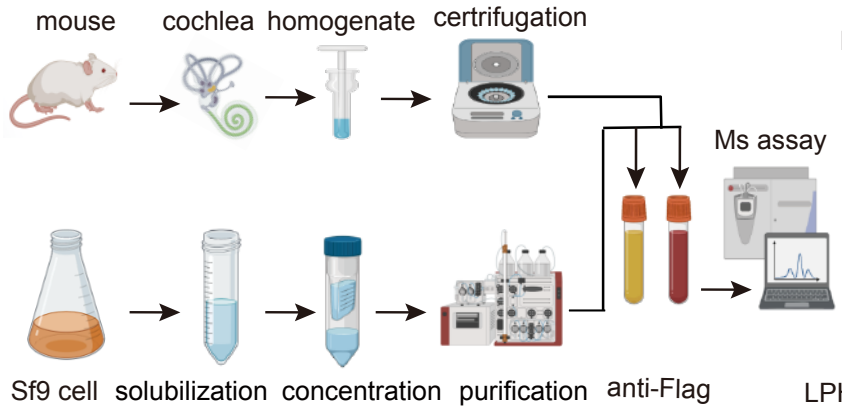

B

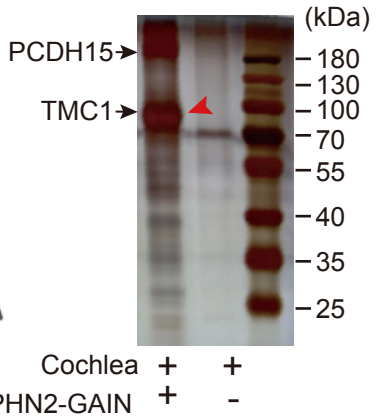

C

LPHN2	+	-
Protein	**Score**	**Score**
TMC1	20.1	NA
PCDH15	34.5	NA

D

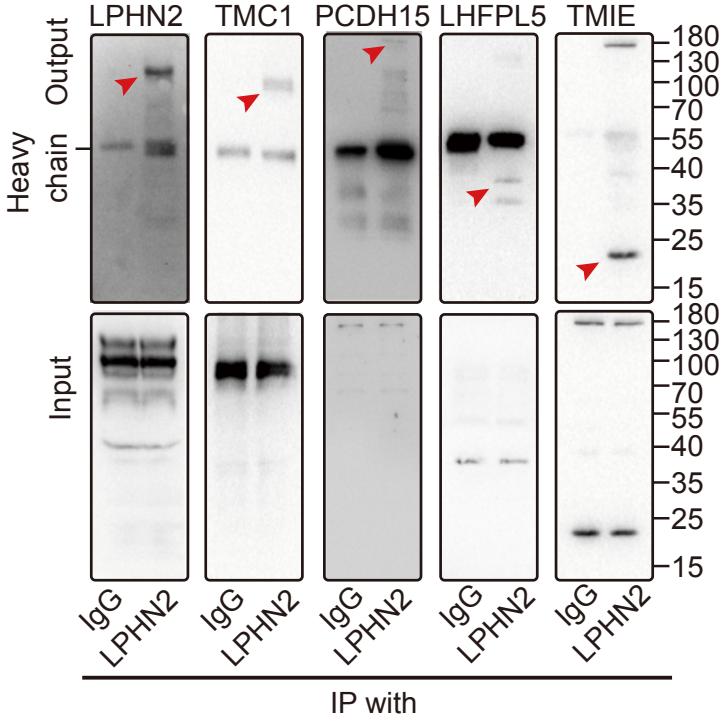

E

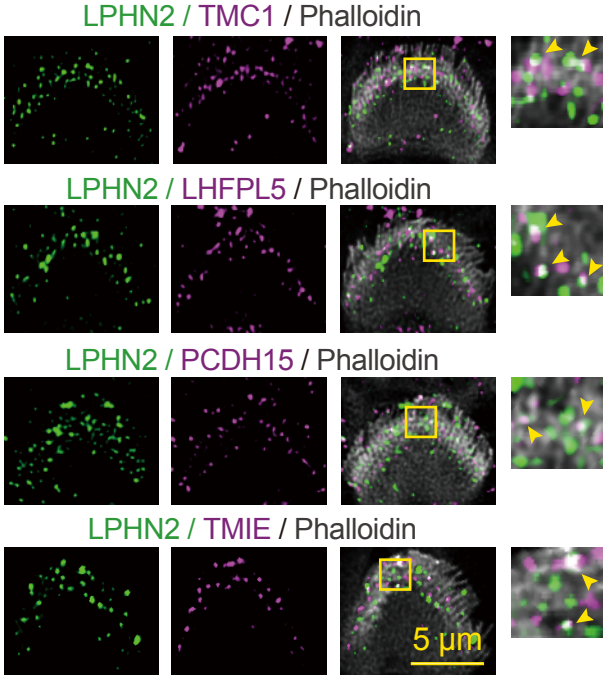

F

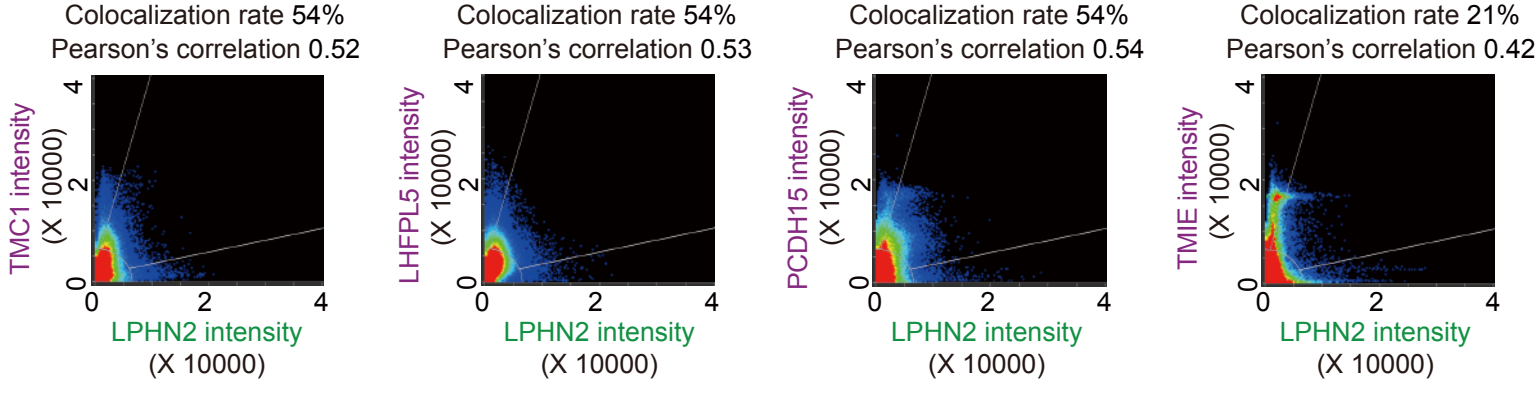

Figure 8

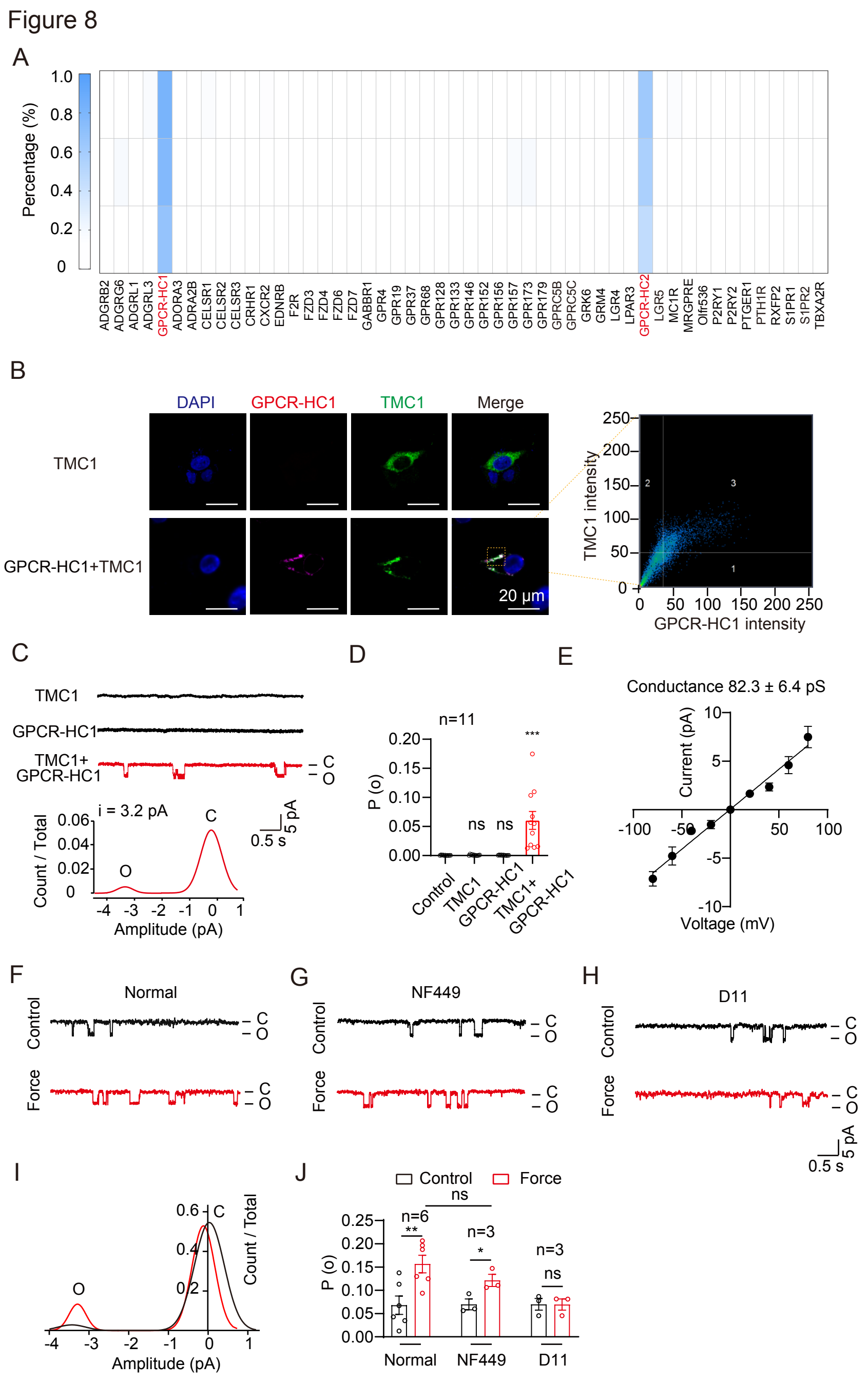
A
Percentage (%)
1.0
0.8
0.6
0.4
0.2
0
ADGRB2
ADGRG6
ADGRL1
ADGRL3
GPCR-HC1
ADORA3
ADRA2B
CELSR1
CELSR2
CELSR3
CRHR1
CXCR2
EDNRB
F2R
FZD3
FZD4
FZD6
FZD7
GABBR1
GPR4
GPR19
GPR37
GPR68
GPR128
GPR133
GPR146
GPR152
GPR156
GPR157
GPR173
GPR179
GPRC5B
GPRC5C
GRK6
GRM4
LGR4
LPAR3
GPCR-HC2
LGR5
MC1R
MRGPRE
Olfr536
P2RY1
P2RY2
PTGER1
PTH1R
RXFP2
S1PR1
S1PR2
TBXA2R
B
DAPI
GPCR-HC1
TMC1
Merge
TMC1
GPCR-HC1+TMC1
20 μm
TMC1 intensity
GPCR-HC1 intensity
250
200
150
100
50
0
0
50
100
150
200
250
1
2
3
C
TMC1
GPCR-HC1
TMC1+
GPCR-HC1
C
O
i = 3.2 pA
Count / Total
0.06
0.04
0.02
0
O
C
-4
-3
-2
-1
0
1
Amplitude (pA)
5 pA
0.5 s
D
n=11
P (o)
0.20
0.15
0.10
0.05
0.00
ns
ns
***
Control
TMC1
GPCR-HC1
TMC1+
GPCR-HC1
E
Conductance 82.3 ± 6.4 pS
Current (pA)
10
5
-5
-10
-100
-50
50
100
Voltage (mV)
F
Normal
Control
Force
C
O
G
NF449
Control
Force
C
O
H
D11
Control
Force
C
O
5 pA
0.5 s
I
Count / Total
0.6
0.4
0.2
C
O
-4
-3
-2
-1
0
1
Amplitude (pA)
J
Control
Force
ns
n=6
**
n=3
*
n=3
ns
P (o)
0.25
0.20
0.15
0.10
0.05
0.00
Normal
NF449
D11

Figure 9

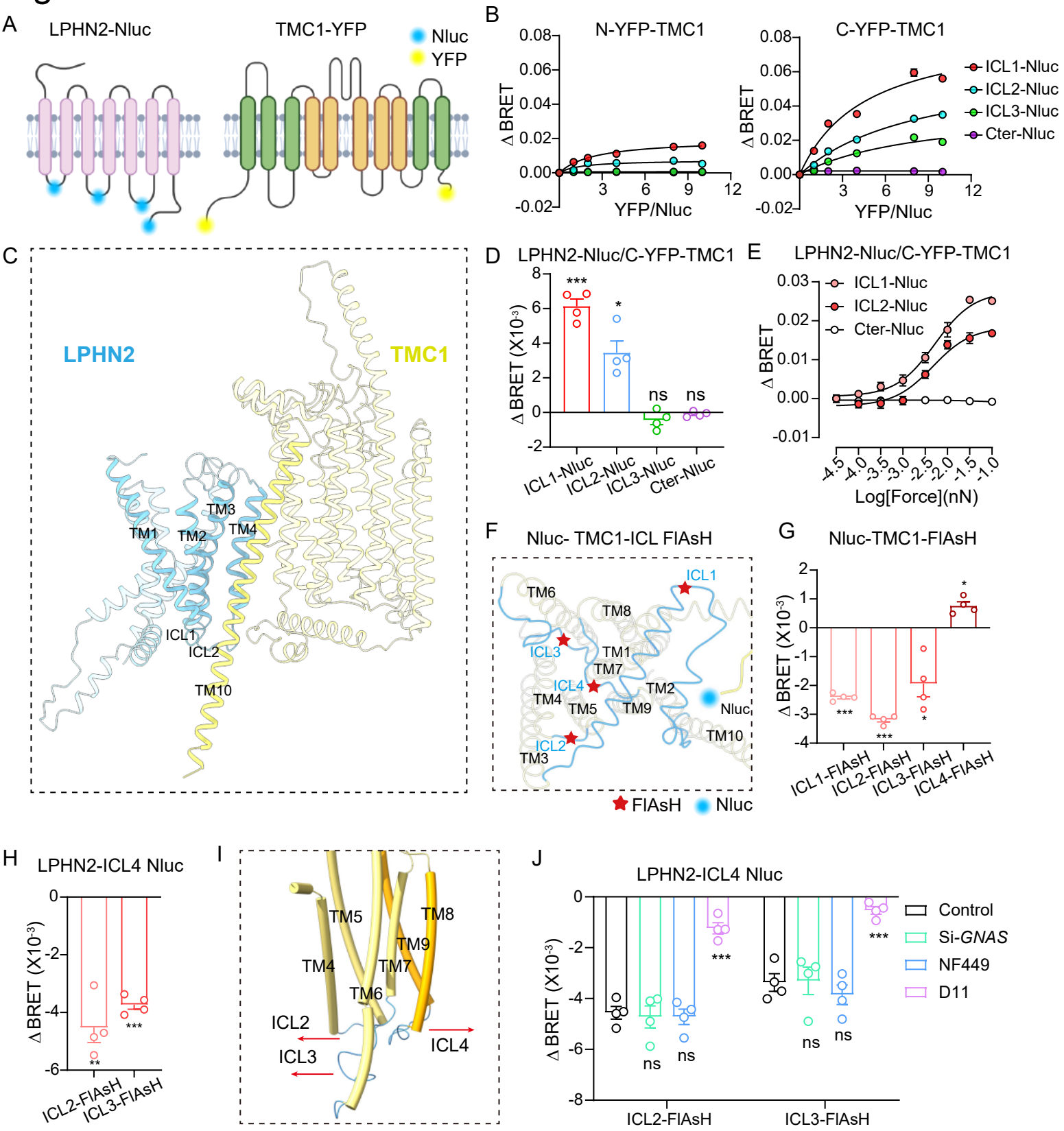
A
LPHN2-Nluc
TMC1-YFP
Nluc
YFP
B
N-YFP-TMC1
C-YFP-TMC1
Δ BRET
YFP/Nluc
ICL1-Nluc
ICL2-Nluc
ICL3-Nluc
Cter-Nluc
C
LPHN2
TMC1
TM1
TM2
TM3
TM4
ICL1
ICL2
TM10
D
LPHN2-Nluc/C-YFP-TMC1
Δ BRET (X10⁻³)
ICL1-Nluc
ICL2-Nluc
ICL3-Nluc
Cter-Nluc
E
LPHN2-Nluc/C-YFP-TMC1
Log[Force](nN)
F
Nluc- TMC1-ICL FlAsH
ICL1
ICL2
ICL3
ICL4
TM1
TM2
TM3
TM4
TM5
TM6
TM7
TM8
TM9
TM10
Nluc
FlAsH
G
Nluc-TMC1-FlAsH
ICL1-FlAsH
ICL2-FlAsH
ICL3-FlAsH
ICL4-FlAsH
H
LPHN2-ICL4 Nluc
ICL2-FlAsH
ICL3-FlAsH
I
TM5
TM8
TM9
TM4
TM7
TM6
ICL2
ICL3
ICL4
J
LPHN2-ICL4 Nluc
Control
Si-GNAS
NF449
D11
ICL2-FlAsH
ICL3-FlAsH

Figure 10

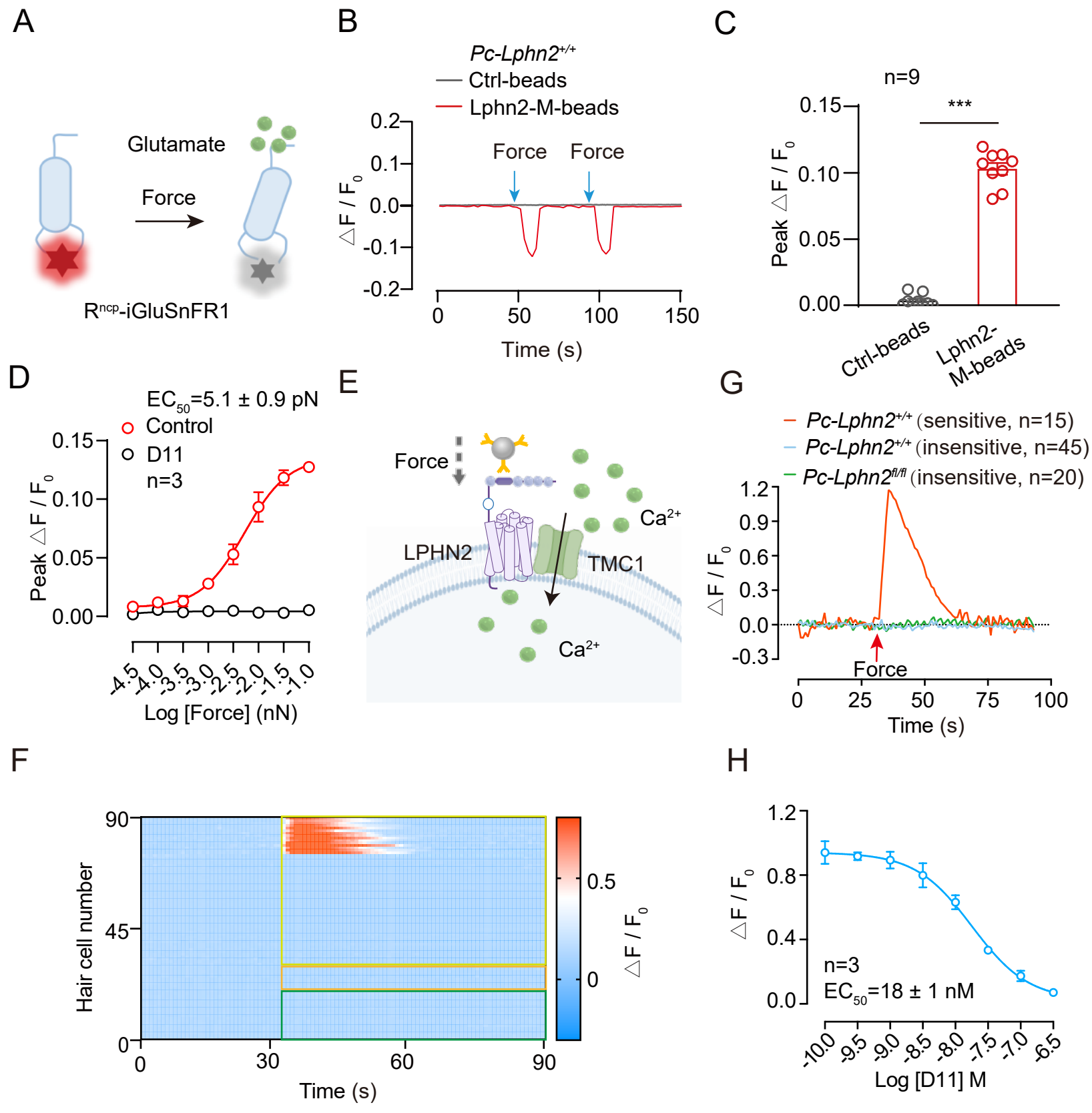
A
Glutamate
Force
Rncp-iGluSnFR1
B
Pc-Lphn2+/+
Ctrl-beads
Lphn2-M-beads
Force
Force
△F / F0
Time (s)
C
n=9
***
Peak △F / F0
Ctrl-beads
Lphn2-M-beads
D
EC50=5.1 ± 0.9 pN
Control
D11
n=3
Peak △F / F0
Log [Force] (nN)
E
Force
LPHN2
TMC1
Ca2+
Ca2+
G
Pc-Lphn2+/+ (sensitive, n=15)
Pc-Lphn2+/+ (insensitive, n=45)
Pc-Lphn2fl/fl (insensitive, n=20)
△F / F0
Force
Time (s)
F
Hair cell number
Time (s)
△F / F0
H
△F / F0
n=3
EC50=18 ± 1 nM
Log [D11] M

Figure 11

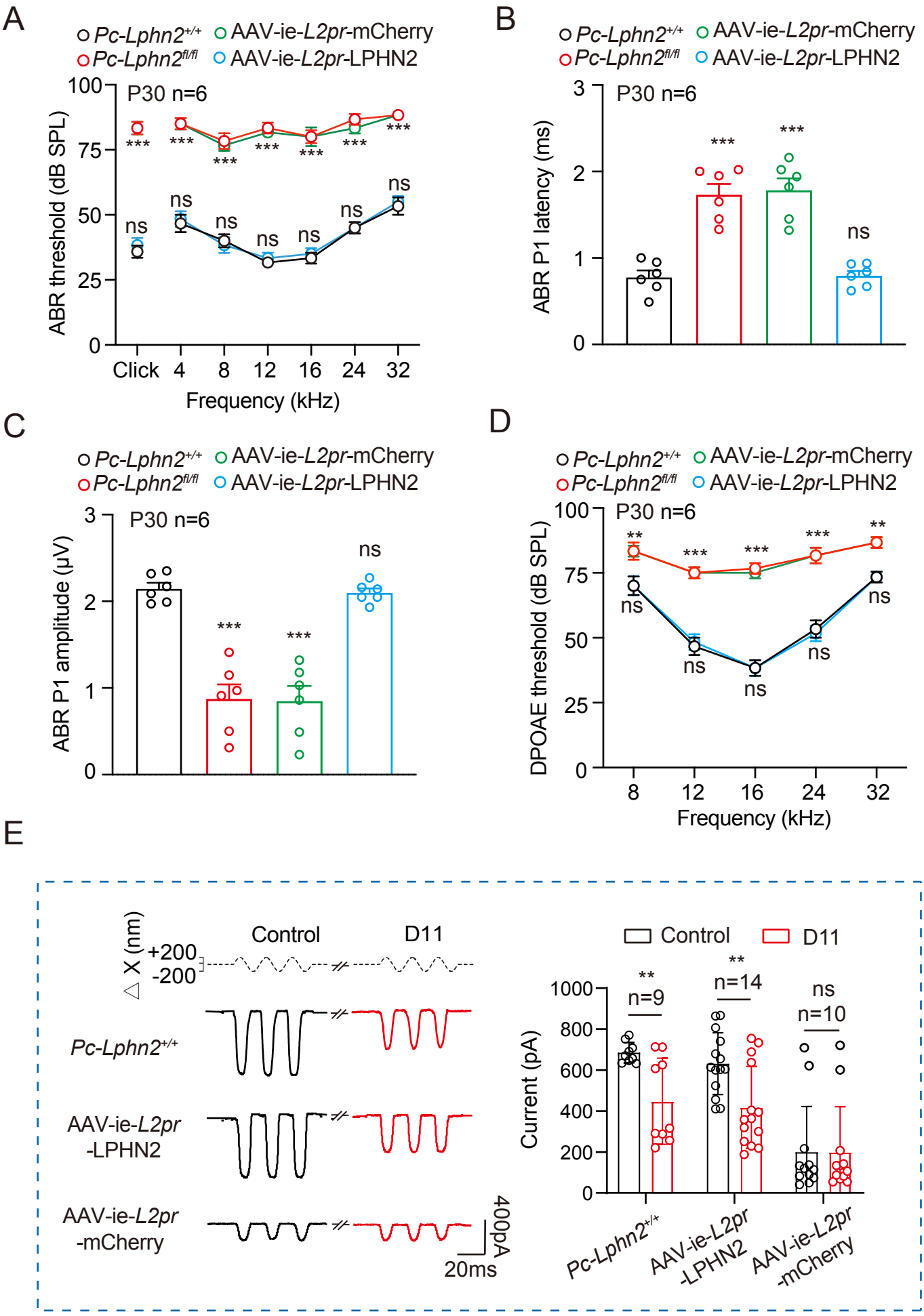
A
Pc-Lphn2+/+
Pc-Lphn2fl/fl
AAV-ie-L2pr-mCherry
AAV-ie-L2pr-LPHN2
P30 n=6
ABR threshold (dB SPL)
Frequency (kHz)
Click
4
8
12
16
24
32
B
ABR P1 latency (ms)
C
ABR P1 amplitude (μV)
D
DPOAE threshold (dB SPL)
E
Control
D11
△X (nm)
+200
-200
Pc-Lphn2+/+
AAV-ie-L2pr -LPHN2
AAV-ie-L2pr -mCherry
400pA
20ms
Current (pA)
n=9
n=14
n=10